Using subthreshold events to characterize the functional architecture of electrically coupled networks

Yaara Lefler [1,2], Oren Amsalem [1], Idan Segev [1] and Yosef Yarom [1]

1. Department of Neurobiology, Institute of Life Sciences and the Edmond and Lily Safra Center for Brain Sciences, The Hebrew University of Jerusalem, Jerusalem, 9190401, Israel.
2. Current address: UCL Sainsbury Wellcome Centre for Neural Circuits and Behaviour, London, W1T 4JG, UK

Y. Lefler and O. Amsalem contributed equally to this work

Corresponding author: Y. Lefler

Abstract

The electrical connectivity in the inferior olive (IO) nucleus plays an important role in generating well-timed spiking activity. Here we combined electrophysiological and computational approaches to assess the functional organization of mice IO nucleus. Spontaneous fast and slow subthreshold events were commonly encountered during in vitro recordings. We show that the fast events represent a regenerative response in unique excitable spine-like structures in the axon hillock, whereas the slow events reflect the electrical connectivity between neurons ('spikelets'). Recordings from cell pairs revealed the synchronized occurrence of distinct groups of spikelets; their rate and distribution enabled an accurate estimation of the number of connected cells and is suggestive of a clustered organization. This study thus provides a new perspective on the functional and structural organization of the olivary nucleus, insights into two different subthreshold non-synaptic events, and a novel experimental and theoretical approach to the study of electrically-coupled networks.

Introduction

In recent years research has confirmed that electrically coupled neural networks are found in every major region of the central nervous system (Condorelli *et al.*, 2000; M. V. . Bennett and Zukin, 2004; Connors and Long, 2004; Hormuzdi *et al.*, 2004). One common feature of these networks is their synchronized rhythmic activity (Connors and Long, 2004; M. V. L. Bennett and Zukin, 2004; Connors, 2017; Coulon and Landisman, 2017) which has been shown to be correlated with higher brain functions such as states of arousal, awareness, cognition, and attention (Ritz and Sejnowski, 1997; Engel, Fries and Singer, 2001; Buzsáki, 2005; Steriade, 2006; Uhlhaas *et al.*, 2009; Wang, 2010). Recently it has been demonstrated that the efficiency of electrical synapses is modulated by electrical and chemical activity, very much like chemical synapses (O'brien, 2014; Marder, Gutierrez and Nusbaum, 2016; Coulon and Landisman, 2017). It thus stands to reason that the functional architecture of these networks must undergo continuous modification to meet system demands. This underscores the urgent need to determine the functional state of a network and associate it with the corresponding brain states. Since anatomical information is insufficient, this can only be done using physiological parameters that capture the functional architecture of a network at any given time.

The inferior olive electrically coupled network, which was among the first networks to be studied in the mammalian brain, provides primary excitatory input to the cerebellar cortex (Eccles, Llinás and Sasaki, 1966). There is a general consensus that the function of this network is to generate synchronous activity of the olivary neurons, which provide temporal information for either learning processes, motor execution, sensory predictions or expectations (Llinas and Sasaki, 1989; Lou and Bloedel, 1992; Welsh *et al.*, 1995; Van Der Giessen *et al.*, 2008; Llinás, 2009; De

63 Zeeuw *et al.*, 2011). Temporal information is thought to be generated by the subthreshold
64 sinusoidal-like oscillations of the membrane voltage that appear to emerge from an interplay
65 between the membrane properties and network connectivity (Llinas and Yarom, 1986; Lampl and
66 Yarom, 1997; Manor *et al.*, 1997; Loewenstein, Yarom and Sompolinsky, 2001; Devor and Yarom,
67 2002b). Recently this oscillatory activity was shown to be governed by synaptic inputs that
68 partially originate in the deep cerebellar nuclei, and modulate the efficacy of the coupling, by
69 defining the spatial extent of the electrically coupled network (Lefler, Yarom and Uusisaari, 2014;
70 Mathy, Clark and Häusser, 2014; Turecek *et al.*, 2014).
71
72 Early work on the morphological organization of the IO indicated that it is organized in clusters
73 of up to 8 neurons, whose dendrites are integrated in glomerulus structures (Sotelo, Llinas and
74 Baker, 1974) and are innervated by both excitatory and inhibitory synaptic inputs (De Zeeuw *et*
75 *al.*, 1990). This presumed cluster organization has been supported by dye coupling studies
76 showing that each olivary neuron is anatomically coupled to roughly ten other neurons (Devor
77 and Yarom, 2002a; Leznik and Llinas, 2005; Placantonakis *et al.*, 2006; Hoge *et al.*, 2011; Turecek
78 *et al.*, 2014). However, the organization of the network has only been addressed physiologically
79 in a few voltage-sensitive dye imaging studies which found ensembles of synchronously active
80 neurons corresponding to a cluster size estimation of hundreds of neurons (Devor and Yarom,
81 2002b; Leznik, Makarenko and Llinas, 2002). The documented synchronicity of complex spikes
82 activity in tens of cerebellar Purkinje cells during motor tasks and sensory stimulation, is also in
83 favor of such of ensemble organization (Bloedel and Ebner, 1984; Welsh *et al.*, 1995; Welsh and
84 Llinás, 1997; Mukamel, Nimmerjahn and Schnitzer, 2009; Ozden *et al.*, 2009; Schultz *et al.*, 2009;
85 De Zeeuw *et al.*, 2011).

In this study, we describe a novel method to estimate the size and efficacy of a network by analyzing the all-or-none subthreshold unitary activity known as a 'spikelet'. Initially, spikelets were considered as the manifestation of an action potential transmitted via electrical synapses (Llinas, Baker and Sotelo, 1974; MacVicar and Dudek, 1981; Valiante *et al.*, 1995; Galarreta and Hestrin, 1999; Gibson, Belerlein and Connors, 1999; Mann-Metzer and Yarom, 1999; Hughes *et al.*, 2002; Chorev and Brecht, 2012). However, in other studies, spikelets were referred to either local dendritic regenerative response (Spencer and Kandel, 1961; Golding and Spruston, 1998; Smith *et al.*, 2013), a reflection of an action potential in the initial segment or at an ectopic site along the axon that fails to invade the soma (Stasheff, Hines and Wilson, 1993; Avoli, Methot and Kawasaki, 1998; Juszczak and Swiergiel, 2009; Sheffield *et al.*, 2011; Dugladze *et al.*, 2012; Michalikova, Remme and Kempter, 2017), an electrical coupling between axons (Schmitz *et al.*, 2001; Traub *et al.*, 2002) or simply extracellularly recorded activity of nearby neurons (Vigmond *et al.*, 1997; Scholl *et al.*, 2015). Here we show that the spontaneous unitary events recorded from olivary neurons can be classified into two groups that differ in their waveform and properties: fast events having identical waveforms with variable high amplitudes, and slow events having different waveforms and low amplitudes. We show that the low amplitude slow events reflect the occurrence of action potentials in electrically coupled neurons, whereas the high amplitude fast events are regenerative responses that are likely to represent action potentials that occur at the axonal spines. We then used the slow events that were simultaneously recorded in pairs of neurons to estimate the number of neurons in the network. We found that each olivary neuron is electrically connected to an average of 19 other neurons

and that the network is not randomly connected, rather it is composed of functional clusters of connected neurons.

Results

Spontaneous unitary events recorded in neurons of the inferior olive.

The subthreshold spontaneous activity recorded from IO neurons (Figure 1A) was characterized by unitary unipolar events that varied in amplitude and waveform. This spontaneous activity, which was observed in 74.3% of the neurons (188 out of 253) with an average rate of 0.7±0.6 /sec (calculated in 70 neurons) were also encountered in the presence of excitatory synaptic blockers (CNQX and/or APV, n=19) although the frequency of occurrence was reduced to an average below 0.02 Hz. These subthreshold events could readily be divided into two populations of small and large events (Figure 1A inset, circles vs. stars), as shown by the amplitude histogram (Figure 1B). K- means clustering of the event waveforms reveals 5 distinct groups (Figure 1C), which when normalized (Figure 1D) showed the waveform difference between the two types; one type had high amplitude and fast kinetics, and the second type had low amplitude and slow kinetics.

To further analyze the event waveforms, we measured each event's rise time and duration at half amplitude. The results obtained from a representative neuron are summarized in Figure 1 E-G. One type (black to grey circles) had a relatively high amplitude (2.4-16.6 mV; average of 7.5±3.1 mV) and fast kinetics (average rise time of 1.3±0.3 ms and average half duration of 3.4±0.3 ms) whereas the second type (purple circles) had a relatively low amplitude (<2mV: 0.6-1.9 mV; average of 1.17±0.3 mV) and slow kinetics (average rise time of 2.4±0.4 ms and average half duration of 11.8±5 ms). Plotting the duration as a function of the rise time (Figure 1G), which

129 further supports the two-type scheme, failed to demonstrate a monotonous relationship
130 between the dendritic location of the synapse and the rise-time/half-width expected from Rall's
131 cable theory (Rall, 1967). Thus, it seems unlikely that the two types represent signals arising from
132 different locations along the cell's morphological structure. The distribution of rise-time and half-
133 width in a population of 49 neurons, which is summarized in Figure 1H-J, confirms that there
134 were indeed two distinct types of events. Whereas the high amplitudes events had a fast rise
135 time (0.8-2.8 ms; average of 1.4±0.4 ms) and short duration (2.5-8.3 ms; average of 4.2±1.3 ms),
136 the low amplitude events had a longer rise time (1.3-4.3 ms; average of 2.5±0.6 ms) and a longer
137 duration (3.6-21 ms; average of 12.7±3.9 ms). For the high-amplitude events, the broad
138 distribution of amplitudes (ranging from 4.5 to15.3 mV) and the somewhat limited distribution
139 of rise-times and durations strongly indicates that these groups of fast events were generated by
140 a similar mechanism.
141 Overall, the frequency of slow events was four times higher (0.56±0.62 /sec; n=69) than that of
142 the fast events (0.14±0.18 /sec; n=58). It should be noted however, that due to low amplitude
143 and limited resolution, a further division of the slower type was difficult However, in 9
144 experiments, this slow signal could be subdivided into two groups showing similar slow kinetics
145 with different amplitudes (not shown).

146 Slow events reflect electrical coupling between neurons.

147 Whole-cell recordings from pairs of coupled olivary neurons revealed that the post synaptic
148 responses to either spontaneously (Figure 2A) or evoked (Figure 2B) action potentials in one
149 neuron were precisely correlated with depolarizing events in the coupled neuron. Both the
150 spontaneous and the evoked events resembled the spontaneously recorded slow events

depicted in Figure 1. These events had an amplitude of 1.2±0.12 mV, a rise time of 3.7±0.9 ms and a duration of 14.9±4.0 ms, thus well within the range of spontaneously measured slow events. Paired recordings from 36 neurons showed that the amplitudes of the events varied from 0.2 to1.67 mV (average of 0.88±0.51 mV) whereas the average rise times and half durations were 2.95±1.05 ms and 21.43±11.05 ms, respectively, in line with the measured distribution of spontaneously slow events (Figure 1H-J). Importantly, spike-triggered depolarizing events for each pair showed minimal variations. Therefore, the relatively large variability of the spontaneous slow events (Figure 1E-G) is likely to represent action potentials in many neurons that were coupled to the recorded neuron. It should be noted that in these paired recordings we never encountered an evoked postsynaptic response that resembled the fast events depicted in Figure 1.

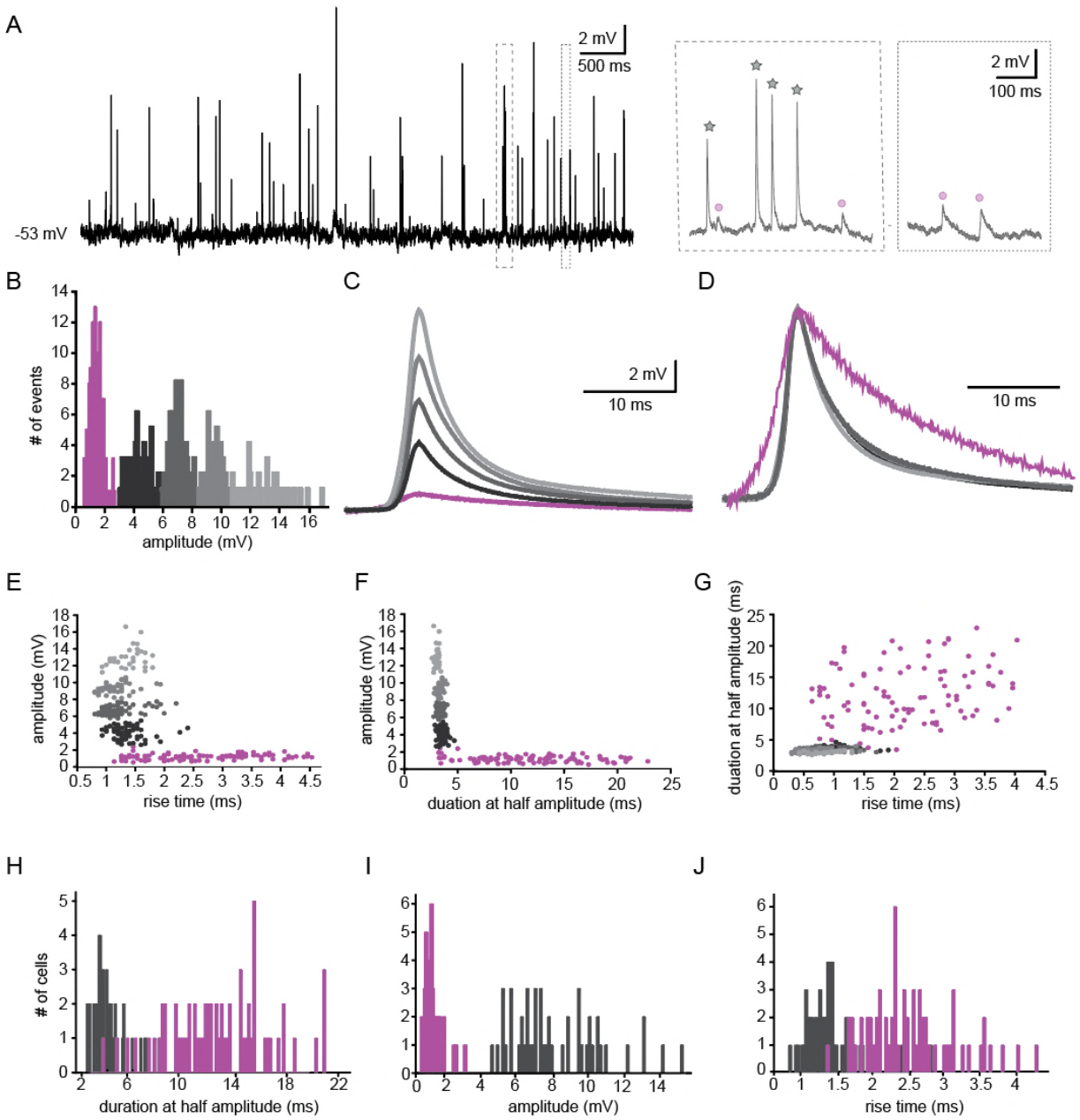

Figure 1. Two types of subthreshold spontaneous events recorded in olivary neurons. (A) Spontaneous subthreshold events recorded from an olivary neuron. Right panels - higher magnification of the marked rectangles; black stars - fast and high amplitude events; purple circles - slow and small events. (B) the distribution of the event amplitudes; colors were assigned according to the K-means analysis of the amplitudes. (C) Averages of the subthreshold events in each cluster, color coded as in B. (D) the normalized events shown in c. (E-G) Scatter plots for the relationships between the shape indices of the subthreshold events (color coded as in B). (E) Amplitude and rise time; (F) Amplitude and half width; (G) half width and rise time. (H-J) Histograms of the shape indices (half width (H); amplitude (I); and rise time (J)) of the subthreshold events in a population of 49 olivary neurons; purple and gray bars correspond to slow and fast events respectively.

163

164 The relatively broad range of spikelet parameters (Figure 1) can be attributed to a wide range of
165 coupling strengths, different locations of the gap-junctions along the dendritic structure or
166 different durations and shapes of the pre-junctional action potential which is a well-known
167 feature of olivary action potentials (Llinás and Yarom, 1981a, 1981b). We first examined the
168 effect of coupling strength by calculating the ratio of the amplitudes of the pre-junctional action
169 potential to the post-junctional spikelet, and compared it to the coupling coefficient measured
170 by direct current injection (see Methods). As shown in Figure 2C, there was a significant positive
171 correlation (with a slope of 0.134; R^2=0.614, p<0.0001; Pearson correlation). Next, we examined
172 the effect of the shape of the pre-junctional action potential on the spikelet parameters. To that
173 end, we partially blocked the voltage dependent potassium current by adding TEA (10mM) to the
174 bath solution. In the presence of TEA, a variety of action potential waveforms were elicited by
175 current injection (Figure 2D). In particular, the initial upstroke of the action potential was
176 unaffected, but there was a significant broadening of the repolarizing phase (Figure 2D, upper
177 panel, dark blue) that often elicited a second calcium-dependent action potential (Figure 2D,
178 upper panel, light blue). This variety of action potential waveforms were always associated with
179 postsynaptic responses that could be clustered into two distinct groups (Figure 2D, lower panel).
180 The prolongation of the action potential was, as expected, followed by a matching increase in the
181 duration of the post-junctional responses (Figure 2D, lower panel, dark blue traces). The
182 appearance of the second component was associated with a slow wave of depolarization in the
183 post-junctional cell (light blue traces). This suggests that the wide range of spikelet parameters

(Figure 1) can be accounted for by the variability in coupling strength and pre-junctional action potential waveforms.

Finally, we examined the occurrence of spikelets in neurons that exhibited subthreshold oscillatory activity. Since these oscillations occurred simultaneously in several neurons (Lefler, Torben-Nielsen and Yarom, 2013), it was expected that spikelet occurrence will be correlated with the oscillatory activity. About 50% of the olivary neurons showed spontaneous subthreshold oscillations (Figure 2E). Careful examination of the peaks of the oscillations (Figure 2F) revealed that they were crowned with spikelets. To quantify this observation, we calculated the distribution of the inter-spikelet-interval (ISLI, Figure 2G, black bars), and found distinct groups appearing at intervals of 200 ms. We then calculated the autocorrelation function of the subthreshold oscillations (Figure 2G, yellow line) and found that it matched the ISLI perfectly. It is important to note that a similar fit was observed in 60% of the oscillating neurons (n=18) whereas in non-oscillating neurons (n=70) the ISLI exhibited a Poisson-like distribution (Figure 2H). The strong correlation between oscillatory behavior and the occurrence of spikelets further supports the conclusion that these events represent activity in adjacent electrically coupled neurons.

To summarize, the observations in Figures 1 and 2 strongly suggest that the small and slow spontaneous events represent action potentials occurring in electrically coupled neurons and therefore we will refer to them as ‘spikelets’.

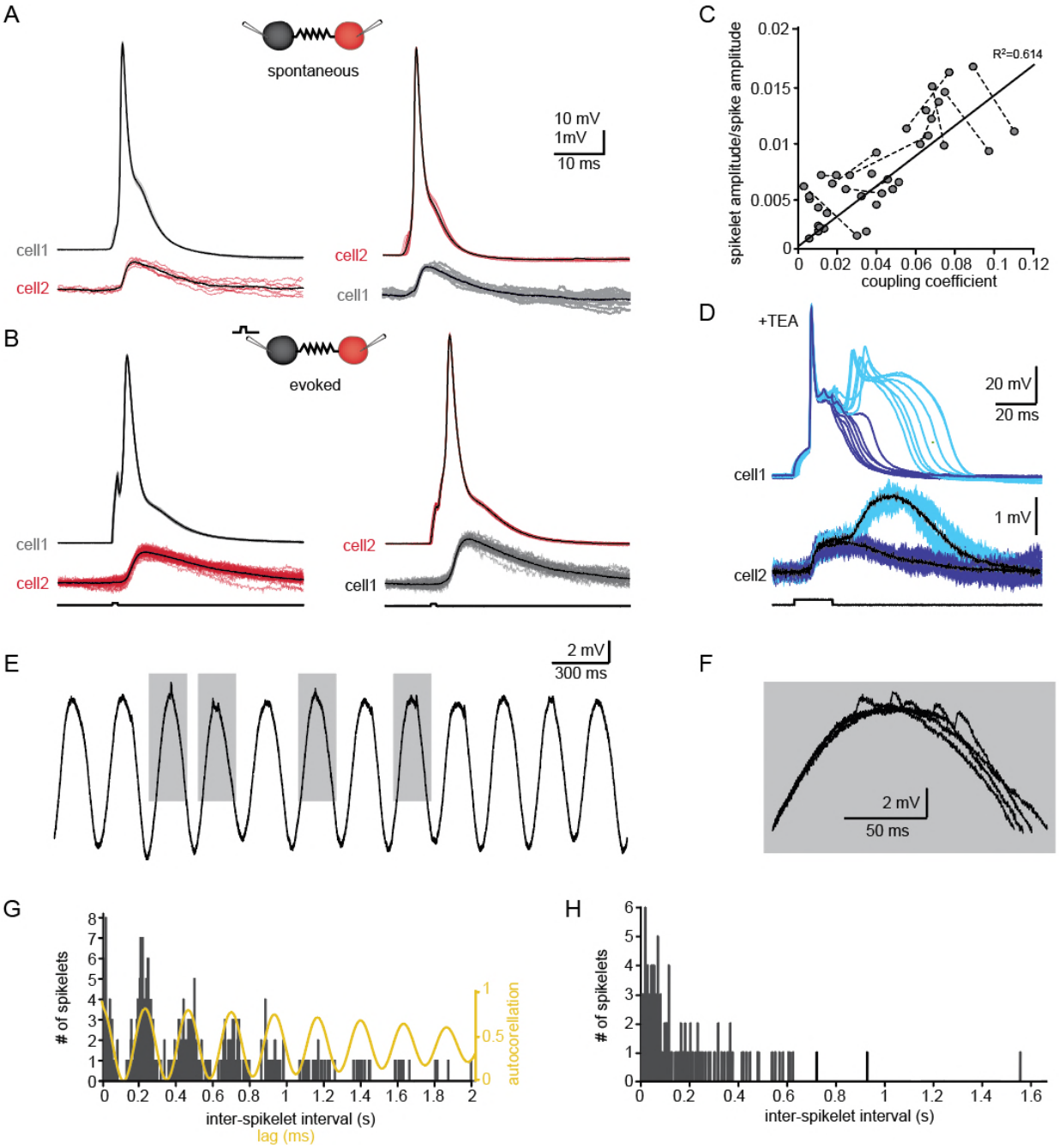

Figure 2. The slow events represent the electrical coupling between neurons. (A) superimposed traces of spontaneously occurring action potentials recorded simultaneously from a pair of coupled neurons (red and gray traces; black traces represent the average events). (B) the same as in A for action potentials evoked by 100 pA, 1 ms current pulses. (C) The linear relationship between the DC coupling coefficient and the spike coupling coefficient. Pairs of cells are connected by dashed lines. Blue line is the linear regression fit (R^2=0.6). (D) Paired recording in the presence of 10mM TEA. Action potentials

with relatively long durations (upper panel, blue traces) were elicited in cell 1 by 50 pA ,20 ms current pulse. Occasionally they were followed by a second response (cyan traces). These action potentials elicited post junctional responses in cell 2 with corresponding waveforms (lower traces). (E) Subthreshold events recorded in oscillating olivary neuron. (F) Superposition of the gray rectangles in E, at higher magnification. Note that spikelets were only present for 50 ms along the peak of the oscillations. (G) Inter-spikelet interval (ISLI) from the same neuron (using 4 ms bins), and an autocorrelation (yellow line) of the membrane potential. (H) The ISLI distribution in a non-oscillating neuron.

205

206 The large and fast events reflect localized regenerative responses.

207 The source of the fast events is a mystery. On the one hand, they seem to be independent of
208 chemical synaptic transmission, and on the other, they are not activated by pre-junctional action
209 potentials in coupled neurons. To resolve this mystery, we first examined the effect of the
210 membrane voltage on the occurrence and waveform of both types of unitary events. We next
211 used an optogenetic approach combined with pharmacological manipulations to gain insights
212 into the source of these events. Finally, we used a computational approach to examine possible
213 mechanisms to account for the experimental observations.

214 The effect of membrane potential was examined by DC current injection, which on average set
215 the membrane potential to a range of -33 to -90mV. Figure 3A-B shows the aligned superimposed
216 traces of spikelets (Figure 3A) and fast events (Figure 3B) from one neuron. Normalizing the event
217 amplitudes (Figure 3A-B, right panels) shows that whereas the spikelet shape was unaffected by
218 the current injection (A), the fast events showed a slowdown of the late repolarizing phase with
219 hyperpolarization (B). Quantifying the effect of the injected current (see Methods) on the
220 amplitude (Figure 3C-D) and duration at 20% of the amplitude (Figure 3E-F) in 16 neurons
221 revealed no effect on the amplitude of either type of events (average slope R^2 = 0.0057 and
222 0.0035, respectively). The spikelet duration was slightly, but not significantly, affected (Figure 3E;

223 R^2 = 0.44; one-sample t-test p=0.057). In contrast, it significantly increased the duration of the
224 fast events (Figure 3F; R^2 = 0.712; one-sample t-test p=0.0005). Comparing the two sets of data
225 revealed a significant difference (Figure 3E vs. F; paired t-test p=0.017). Finally, we measured the
226 effect of the DC current injection on the rate of occurrence of the subthreshold unitary events
227 (Figure 3G-H). Whereas the frequency of the spikelets remained unaffected (Figure 3G, R^2 =
228 0.012), the frequency of the fast events increased by a factor of up to 5 (Figure 3H; R^2 = 0.836).
229 This difference between the occurrence of spikelets and the fast events was highly significant
230 (Figure 3G vs. H, p=0.005, paired t-test). These differences further support our presumption that
231 two different mechanisms generate the two types of subthreshold unitary events. Since spikelets
232 are evoked by action potentials in paired cells, DC current injection to the post-junctional cell will
233 not have a significant effect on the number of action potentials in the pre-junctional cell. On the
234 other hand, the voltage dependency of the fast events strongly suggests that they reflect
235 regenerative responses initiated within the neuron. We therefore refer to them as Internal
236 Regenerative Events or IREs.

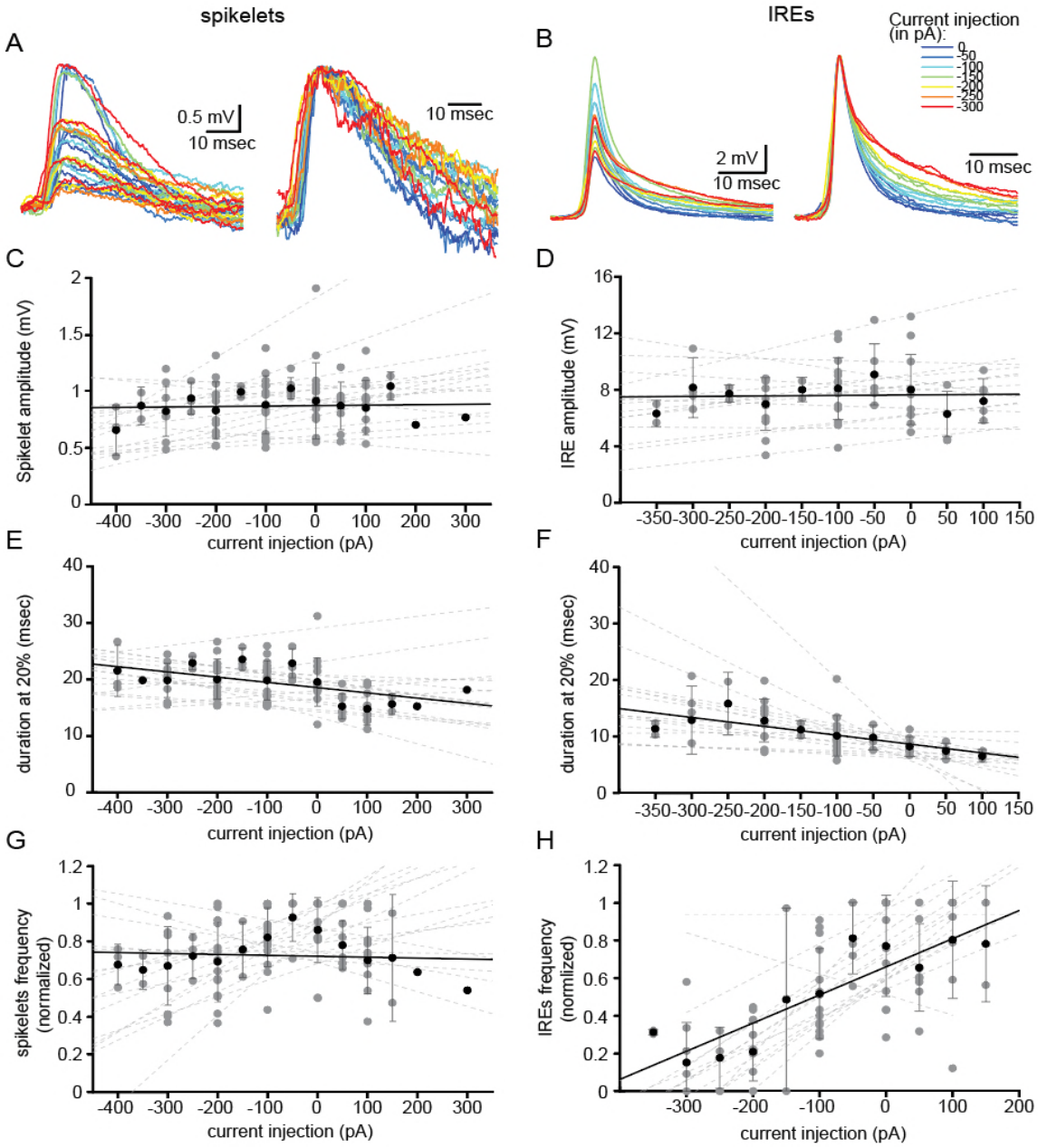

237

Figure 3. Voltage dependency of the subthreshold events. (A) superimposed spikelets recorded during seven different DC current injections (0 to -300 pA, color coded, left panel), and normalized by amplitude (right panel). (B) same as a, for the fast events ('IREs'). (C-H) The effect of DC current injection on the amplitude (C-D), the duration, measured at 20% of the amplitude, (E-F) and the frequency of occurrence (G-H) measured in 16 neurons. Gray circles represent the average data from individual neurons, each fitted with a linear regression (dashed gray lines). Black circles and error bars (std) represent the average value for all the neurons in each current injection. Note that the decrease in duration (F) and the increase in frequency (H) with depolarization only occurs for IREs.

238 Next, we examined the ability of the IREs to trigger a full-blown action potential. Figure 4A shows
239 the superposition of spontaneously occurring action potentials (black and purple traces) and IREs
240 (gray traces) measured from the same neuron. It is clear that some of the action potentials
241 (purple) are preceded by a fast pre-potential that resembles the spontaneous IREs. This
242 possibility was further supported by phase plotting the action potential (Figure 4B, purple and
243 black traces), which showed that 62% of the spontaneous action potentials were triggered by
244 depolarizing events that resembled the IREs in amplitude and waveform. On the population level
245 29.2±26.7% of the IREs triggered action potentials, whereas 41.6±21.2% of the action potentials
246 were triggered by IREs (Figure 4C). It should be noted that this is an underestimation, since action
247 potentials that seem to arise from the baseline might also be evoked by an IRE that is masked by
248 the beginning of the action potential (see inset in Figure 4A).
249
250 We then examined the possibility of activating these events by synaptic inputs, using Thy1-ChR2-
251 YFP transgenic mice in which ChR2 is expressed in axons that deliver excitatory inputs to the IO
252 but not in IO neurons (Lefler, Torben-Nielsen and Yarom, 2013). As shown in Figure 4D, a short
253 light pulse (inset) triggered a compound response comprised of synaptic potentials crowned with
254 fast events that occasionally triggered action potentials. The evoked events were isolated by
255 subtracting the synaptic response (Figure 4E, top panel, gray traces). They were then compared
256 to IREs that occurred spontaneously (middle panel, black traces) by averaging and normalizing
257 each of the groups (lower panel). Whereas the rise time for the spontaneous IREs matched that
258 of the evoked IREs perfectly, the decay of the evoked response was considerably faster. This
259 difference might be the result of a depolarized membrane potential during the synaptic event,

260 which is in line with the effect of DC depolarization on the IRE waveforms (Figure 3), as well as

261 the result of high membrane conductance.

262

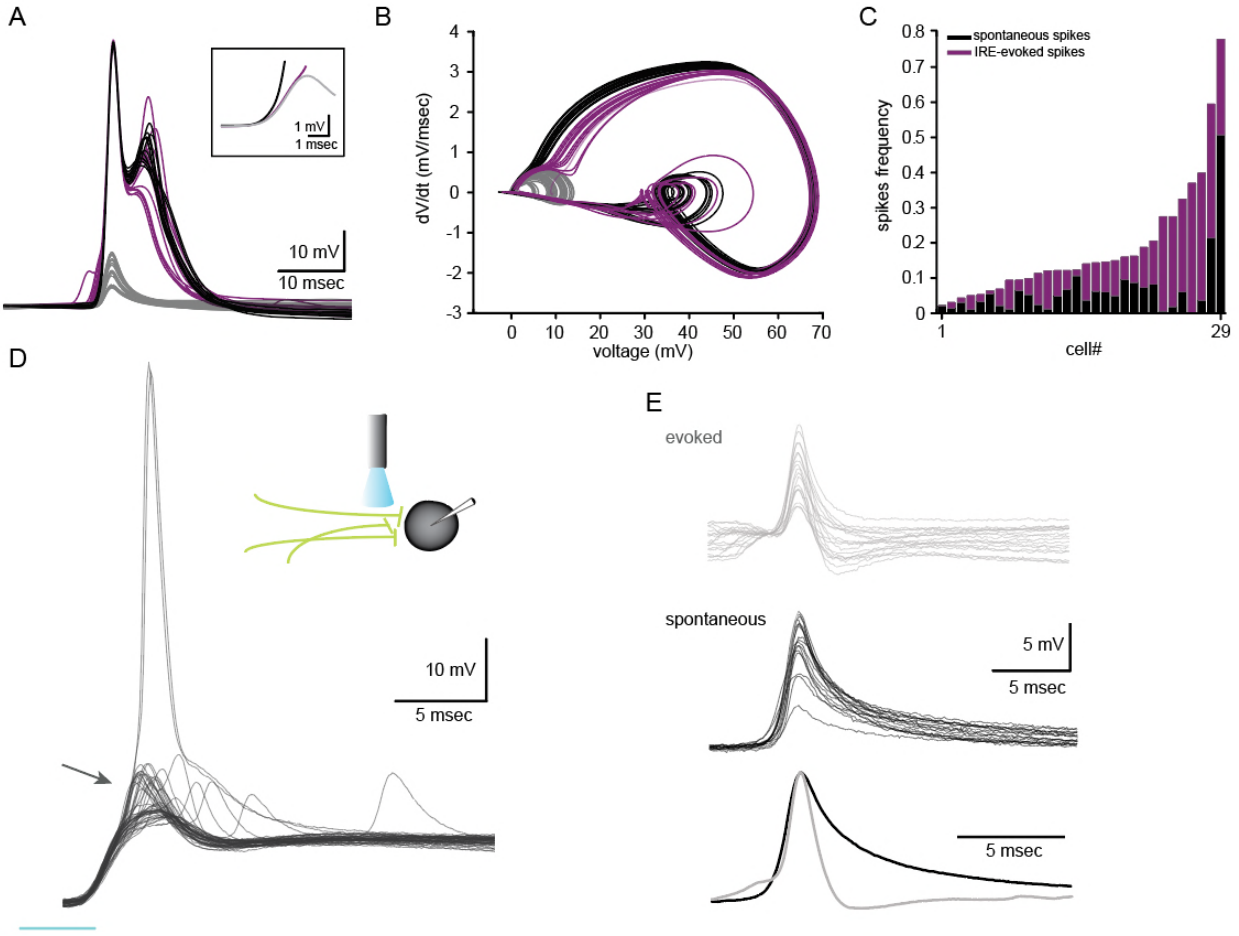

263

Figure 4. Internal Regenerative Events (IREs) are the major source of action potentials and can be evoked by synaptic inputs. (A-B) Voltage (A) and phase plots (B) of spontaneous occurring IREs and action potentials. Purple - action potentials that were triggered by IREs, gray – IREs that failed to trigger an action potential. Black - fast rising action potential. (C) frequency of spontaneous action potentials (black bars) and of IRE-evoked action potentials (purple bars) in 29 neurons. (D) Thy1-ChR-EYFP mice were used to optogenetically activate incoming excitatory axons (inset). Superimposed traces recorded from an olivary neuron in response to 5 ms light pulse, showing synaptic potentials topped with IREs (arrow) that occasionally triggered action potentials. (E) Upper panel: IREs evoked by the synaptic input. Middle panel: spontaneous IREs recorded from the same neuron. Lower panel: normalized average of the spontaneous (black) and the evoked (gray) events. The evoked IREs were isolated by subtracting the average subthreshold synaptic waveform.

264

These results strongly support the possibility that the fast events are generated within the neuron either spontaneously or in response to synaptic input. Their fast kinetic suggests that sodium current is involved; in fact, these fast events were not detected in 27 neurons that were injected with QX-314 (2-5 mM). This contrasts with normal conditions in which only 28% of the cells were devoid of fast events. Furthermore, in a complex experiment with two patch electrodes in the same neuron, one filled with regular intracellular solution and the other with QX (Supplemental information, Figure S1), we found that in the control condition both IREs and spikelets were readily detected (Figure S1A) whereas when breaking into the cell with the QX- containing electrode, the fast events could not be detected whereas the spikelets were almost unchanged (Figure S1B). Finally, in CX 36 knockout mice, where gap junctions were eliminated (De Zeeuw *et al.*, 2003), fast and high amplitude events could still be encountered (Figure S1C). These results strongly confirm our supposition that the fast events are generated within the neuron.

Modelling the Internal Regenerative Events (IREs)

Our experimental observations suggest that IREs represent regenerative responses within the recorded neurons. It was suggested that such responses could result from either dendritic 'hot spots' (Spencer and Kandel, 1961) or from the failure of antidromic axonal spikes at remote Nodes of Ranvier (Traub, Colling and Jefferys, 1995; Avoli, Methot and Kawasaki, 1998). The most characteristic feature of the IREs is that for any given cell, their amplitude clearly segregates into distinct groups, whereas their waveform is essentially identical (Figure 1C-D). We used a modeling approach to explore the conditions in which this feature could be reproduced, either for dendritic 'hot spot' or for axonal spike failure.

To examine the possibility of "dendritic hotspots" we developed detailed compartmental models of three 3D reconstructed olivary neurons; a sample modeled cell is shown in Figure 5A-C. To simulate "hot spots", we injected, at every dendritic location, a simulated spike (Stuart and Sakmann, 1994) with a 100 mV amplitude and a 2 ms half-width (Figure 5D). We searched for the dendritic locations where the resultant somatic voltage response resembled the experimental IREs, with half-widths ranging from 3.25 to 3.5 ms (see Figure 1F). This yielded nine possible confined dendritic locations in the modeled cell (colored dendritic segments in Figure 5C). The respective simulated responses are shown in Figure 5E. Thus, although the amplitudes of these responses varied from 2 mV to 6.5 mV (Figure 5E), their waveforms were almost identical (Figure 5F). Similar results were found in two other modeled cells, thus demonstrating that only well-placed dendritic "hot spots" could replicate the experimental results.

To examine the possibility of axonal spike failure we constructed a model of a myelinated axon connected via an initial segment to an isopotential soma connected to several passive dendrites (Figure 5G; see Methods). We examined the somatic voltage response to an antidromic action potential (activated by short current injection at node 10) during successive blockade of the Nodes of Ranvier (starting with node 1 only, then node 1+2, etc.). As more nodes are blocked, a smaller somatic response is expected (Figure 5H, brown, red, yellow and green traces, respectively). Surprisingly, normalizing the amplitude of these responses (Figure 5I) revealed that the waveform was almost completely unaffected by the location of the propagation block. This was due to the small effective capacitance of the myelin. Indeed, increasing the myelin capacitance enhanced the difference between the waveforms of the somatic responses (Figure 5J-K).

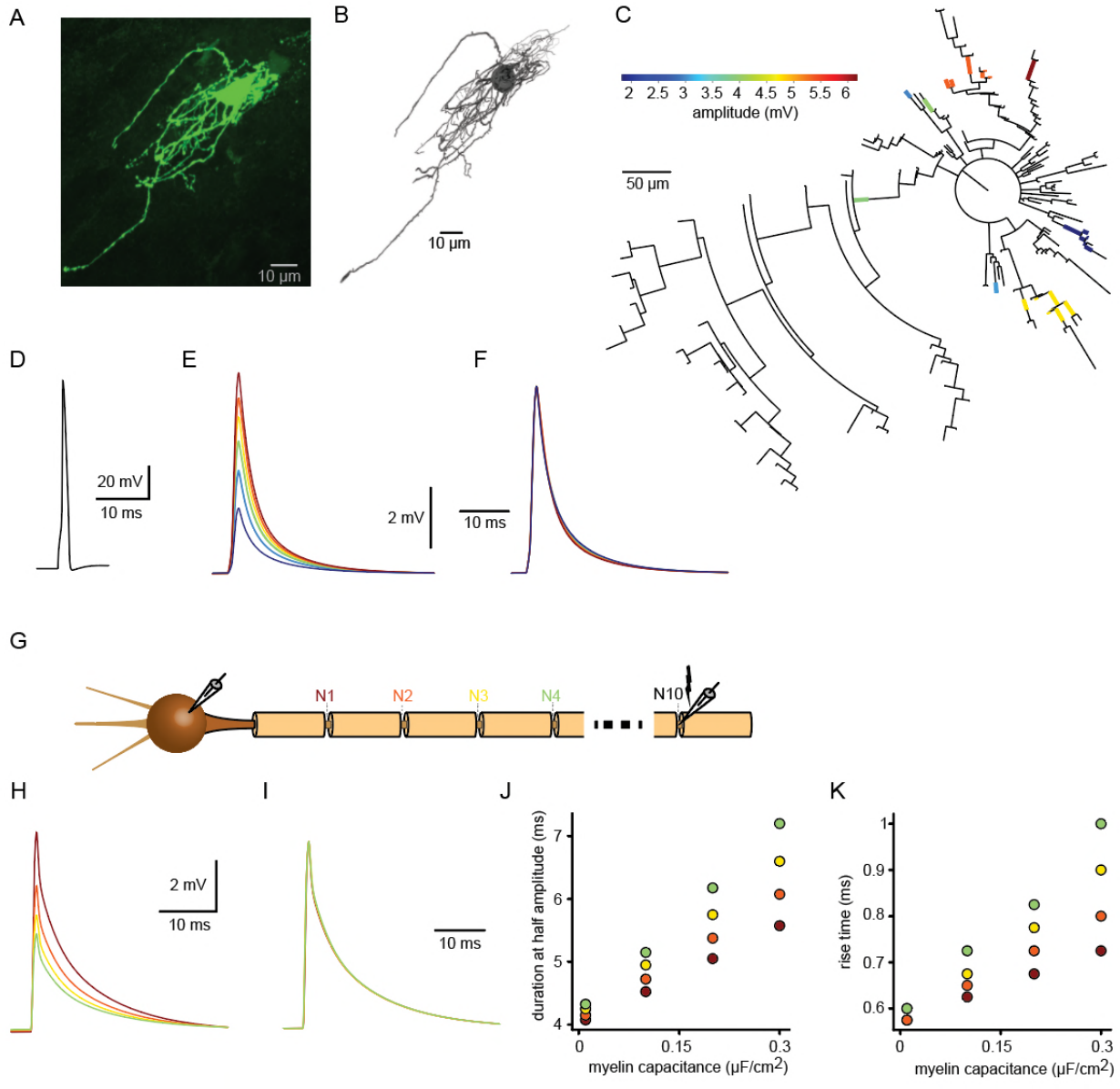

309

Figure 5. Dendritic hotspot (A-F) and axonal failure (G-K) models for the generation of internal regenerative events. (A) Confocal image of a Biocytin filled olivary neuron. (B) 3D reconstruction of the neuron in a. (C) Dendrogram of the reconstructed neuron with possible 'hot spot' locations color coded according to the amplitude of their somatic response (see color bar). (D) the action potential waveform generated in each of the hot spots. (E) The somatic responses to the activation of each hot spot. (F) Normalization of the responses in E. (G) Schematic Illustration of the model consisting of a soma, an axon hillock, an axon initial segment and 10 myelinated segments, separated by active nodes (N1-N10). (H) The somatic responses to failure of the antidromic action potential in N1-N4 (color-coded). (I) Normalization of the responses in H. (J-K) Duration and rise times of the events plotted against the myelin capacitance.

Both models reproduced the characteristic features of the IREs; i.e., identical waveforms and variable amplitudes. However, it is difficult to envisage a biological mechanism that either specifically localizes channels in a restricted dendritic "hot spot" or that simultaneously blocks two, three or more Nodes of Ranvier. Interestingly, however, olivary neurons have unique axons which provide a third possible explanation for the IREs. The classical work by De Zeeuw and colleagues (De Zeeuw *et al.*, 1990) demonstrated the existence of a spine apparatus in the axonal hillock of olivary neurons. We modeled these axonal spines while taking their different neck lengths into account (Figure 6A) and assumed that their head membrane is excitable (see Methods). Figure 6B shows the somatic responses, ranging from 6 to 9 mV, that resulted from action potentials generated in these axonal spines by a short current injection. The somatic responses had identical waveforms (Figure 6C). Importantly, these axonal spines are innervated by excitatory synapses (see De Zeeuw *et al.*, 1990, Figure 9C), enabling their individual activation. We next examined whether the model of excitable axonal spines could replicate the experimental finding that the IREs exhibit an increased duration upon membrane hyperpolarization (Figure 3). The results confirmed that injection of hyperpolarizing or depolarizing currents into the model soma altered the action potential waveform in the spine head (Figure 3D), particularly the after-hyperpolarizing phase, which, as expected, turned into a depolarizing phase (black arrow in Figure 6E, left panel). As a result, the duration of the somatic response increased (red arrow in Figure 6E, right panel). This effect was observed for three levels of somatic current injections (-150 pA, -30 pA and +30 pA) for all four spines (Figure 6F). The normalized responses are displayed in Figure 6G, and illustrate the prolongation of the repolarizing phase of the somatic responses with hyperpolarization, as found experimentally.

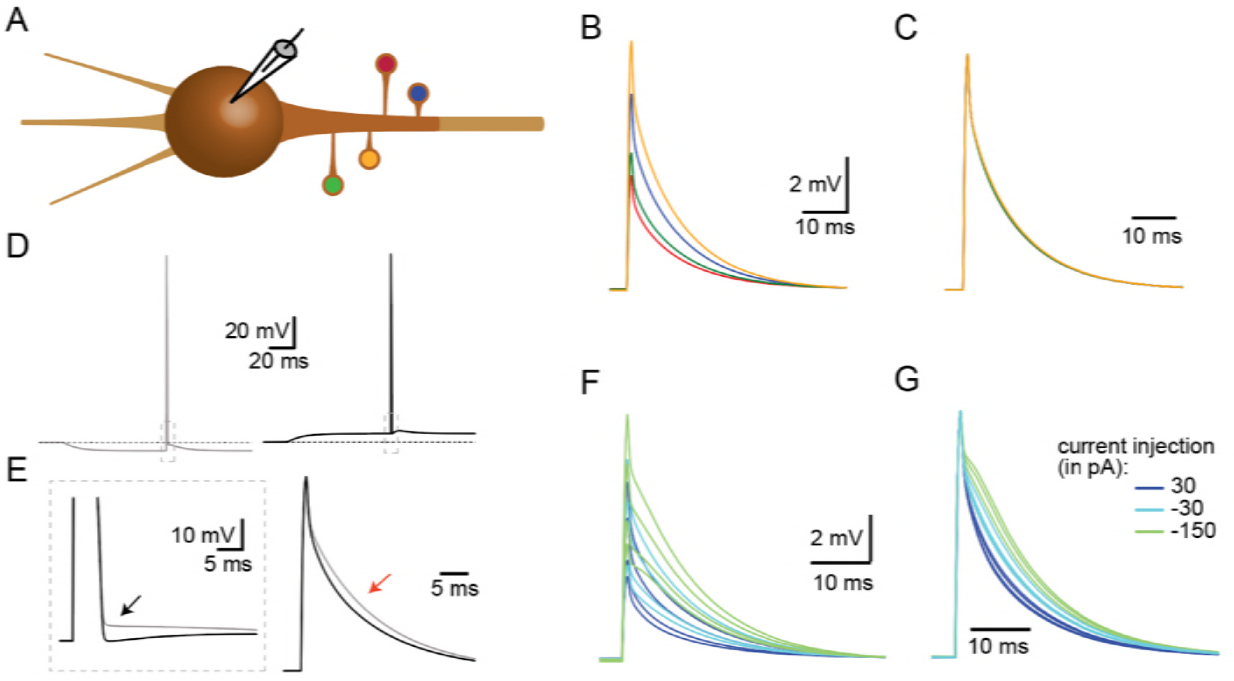

Figure 6. Initial segment spine model for the generation of internal regenerative events. (A) Schematic representation of the model where 4 different spines are located along the axon hillock. (B) Somatic response to action potentials generated in the spine head of the spines (color coded in A). (C) Normalization of the responses in B. (D) The effect of somatic hyperpolarization (gray trace, left panel) and depolarization (black trace, right panel) on the action potential waveforms. (E) left panel, Superposition of the dashed rectangles of the action potentials in d and e showing the difference in the after-hyperpolarization (black arrow) between hyperpolarization and depolarization. Right panel, Superposition of the somatic responses showing the prolongation of the response with hyperpolarization (red arrow). (F) Somatic response evoked by spine action potentials at three levels of somatic DC current injection. (G) Normalization of the responses in F.

Estimating network architecture from dual cell recordings of simultaneously occurring spikelets.

Figure 7A depicts the spontaneous activity recorded simultaneously from two neurons. As described above (Figure 2) action potentials (diagonal bars) that occurred irregularly in either of the two neurons were always associated with spikelets in the paired neuron (Figure 7B). The subthreshold activity, which was dominated by spikelets as well as IREs, appeared randomly in the two neurons. However, occasionally spikelets occurred simultaneously in both cells (marked in Figure 7A and shown at high resolution in Figure 7C) which we refer to as 'common spikelets'.

Each of the three examples shown in Figure 7C, which occurred without measurable time difference, have variable amplitudes. The first and the third spikelets had larger amplitudes in the red neuron (cell 2) whereas the middle spikelet had a larger amplitude in the black neuron (cell 1). Since action potentials in one neuron evoke very similar spikelets in the other (Figure 2A-B), the most likely explanation is that each of these common spikelets represents the action potential in an additional neuron that is coupled to both of the recorded neurons (see Discussion). On the population level, 18 out of 38 pairs had common spikelets (47%). Of these pairs, the occurrence of common spikelets varied from 0.02 to 1.1 /sec, which is 3.5- 66% of the total number of measurable spikelets (Figure 7D).

The occurrence of common spikelets can be used to estimate the number of neurons that are electrically coupled to each neuron in the olivary network. In this example of a paired recording, 4 different groups were identified by clustering the detected common spikelets by the amplitude value and amplitude ratio between the two neurons (Figure 7E), which indicates that at least 4 neurons were electrically coupled to both recorded neurons. Further analysis of these data provided an estimate of the total number of neurons connected to each of the 2 recorded neurons: in this example, 16 common spikelets in 4 groups were recorded; in other words, these neurons fired on average 4 times during the recording period. Since 25 and 50 spikelets were recorded overall for the black and red neuron, respectively, the 9 and 32 non-common spikelets argue for the presence of additional electrically coupled neurons. Assuming that all the neurons fired at similar rates (~4 spikes during the recording period), these non-common spikelets thus represent spikes in 2 additional neurons connected to the black neuron and 8 neurons connected to the red neuron. The result of this numerical consideration is that the black neuron is connected

363 to the red neuron, to 4 additional neurons that are connected to both recorded neurons and an
364 estimated 2 additional neurons, thus totaling 7 neurons. Similarly, the red neuron is connected
365 to up to 13 neurons. This analysis was performed on 18 dual recordings and the results, which
366 are summarized in Figure 7F, indicate that a neuron can connect to as many as 40 other neurons
367 (average of 19.2±10.3). It should be noted that the use of a slice preparation undoubtedly
368 contributed to the wide range of connected neurons and to some degree of underestimation (see
369 Discussion).
370 Further insights into the organization of the network can be extracted from the distribution of
371 the number of groups of common spikelets. As shown in Figure 7G, the number of common
372 groups varied from 0 to 7 with a likely higher incidence at 2 - 4 groups. As will be shown below,
373 this type of distribution cannot be the result of random connectivity where the probability of
374 connection depends solely on the distance between the recorded cells.

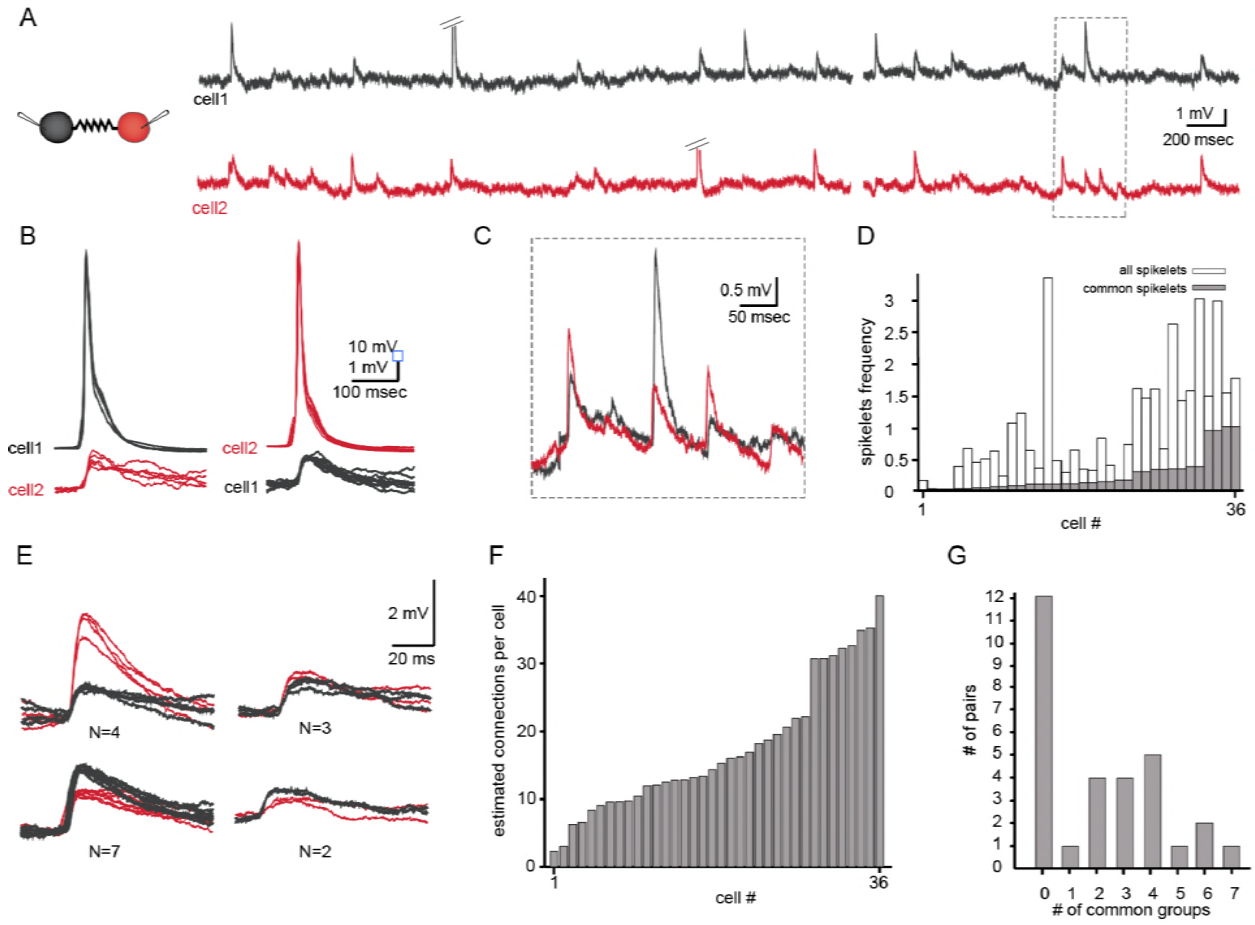

Figure 7. Common groups of spikelets during paired recording reveals the average number of neurons that are electrically coupled to each neuron in the slice. (A) Simultaneous recording from two electrically coupled neurons. Action potentials were truncated (doubled diagonal lines) and an example of the occurrence of common spikelets is marked (dashed rectangle). (B) Superimposed traces of spontaneous action potentials in either cell 1 (black neuron) or cell 2 (red neuron) and the corresponding spikelets in the other neuron. (C) Higher magnification of the rectangle marked in A, showing spikelets that occur simultaneously in both neurons. (D) Histogram of the frequency of spikelets in neurons recorded in pairs, showing all the spikelets (white bars) and all the common spikelets (gray bars; n=18 pairs). (E) Example of common spikelets from the pair presented in a-c. The spikelets could be divided into 4 groups, with N = 2-7 spikelets in each group. (F) Histogram of the estimated number of neurons that are electrically coupled to each of the pair-recorded neurons (n=18 pairs). (G) The distribution of the number of common groups in all recorded pairs.

We re-examined the approach we used to estimate the number of connections per neuron by reconstructing a realistic olivary network (Figure 8A, see Methods). The firing rate of neurons in

379 the network was set to 0.058 Hz ± 0.04 Hz (as observed experimentally) and the number of
380 common spikelets in pairs of neurons occurring within 15 min of simulation was measured.
381 Recordings from a sample pair are shown Figure 8B. In this example, four groups of spikelets that
382 appear 26, 16, 65 and 32 times were detected (Figure 8B). By applying the same calculation as
383 performed in the experimental observations (Figure 7), we concluded that the red neuron was
384 electrically connected to 24 neurons whereas the black neuron was connected 26 neurons. In
385 this model, the red and black neurons were actually connected to 17 and 20 neurons, respectively
386 (pink circles in Figure 8C). We performed the same calculation in 20 randomly selected pairs of
387 neurons and plotted the estimated versus the real number of connections per cell (Figure 8C).
388 The results were distributed along the diagonal, (with the average marked by + sign), thus
389 demonstrating the validity of this approach in estimating the number of connections for each
390 neuron. However, the accuracy of the estimation depends strongly on the variability in firing rate
391 and the recording duration; the accuracy decreases the shorter the recording duration and the
392 higher the firing rate variability, but the error in estimating the average number of connections
393 for each cell was still small (Supplemental information, Figure S2, see discussion).
394 The experimental distribution of the number of groups of common spikelets (Figure 7G) provides
395 additional information on the organization of the network. We examined two possible
396 connectivity patterns that might support this type of distribution (see Methods; network
397 connectivity matrices). The first is a network where the probability of a connection between two
398 neurons depend solely on their inter-somatic distance (Figure 8D). The second assumes that the
399 network is organized into clusters of neurons (Figure 8G), where the connection probability
400 within a cluster is larger than between clusters (both probabilities are distance-dependent). We

searched for the parameters that yielded the best fit to the experimental observations; namely, the distance-dependent connection probability (see Devor and Yarom, 2002a and Figure 8E, H) and the distribution of common neighbor (proxy for groups of common spikelets in Figure 8F, I). Our search yielded an interesting result. Whereas the simple distance-dependent network captured the distance-dependent probability of a connection (Figure 8E), it failed to reproduce the distribution of common groups as found experimentally (Figure 8F). On the other hand, when the modeled networks were organized in clusters, it replicated both the experimental distribution of common groups (Figure 8I) as well as the distance-dependent connection probability (Figure 8H). Note that in all modeled networks, each neuron was connected to about 11-21 neurons, which lay within the numbers estimated from the experimental observations (Figure 7F).

Figure 8 also shows that the experimental results could be reproduced in networks with various distance-dependent connectivity profiles (see Methods), provided that the network is organized into clusters of neurons. Figure 8 H-I presents two examples of networks that differ in their within- and between- connectivity profiles (black vs. gray lines in Figure 8H inset). The resultant distance-dependent connectivity and the distribution of the common groups for these two cases are denoted by the black and gray bars. Thus, it seems likely that the inferior olive is organized into clusters of neurons with a higher probability of connection within clusters and a low connection probability between clusters.

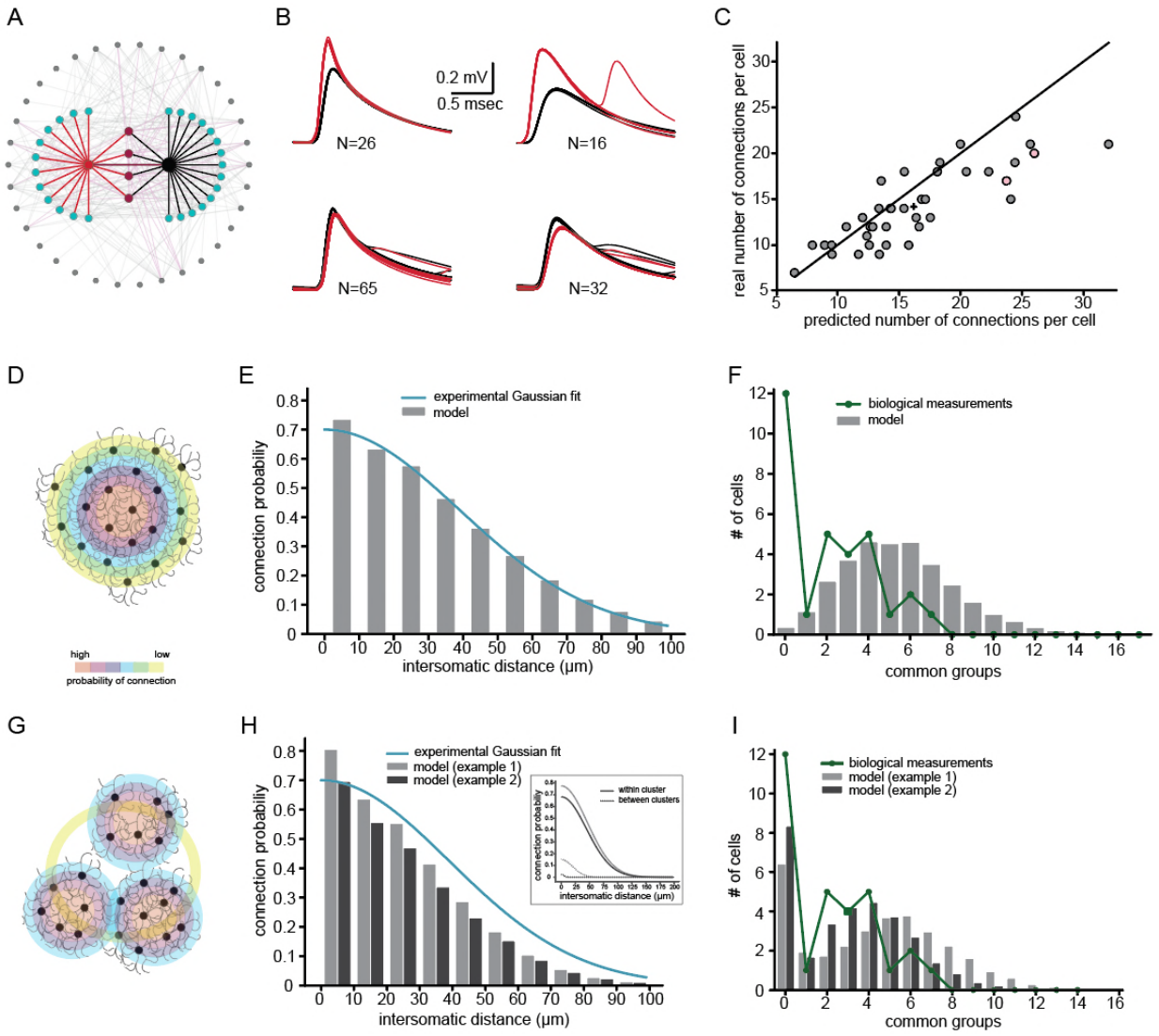

420

Figure 8. Simulations examining both the method used for estimating the number of connections per cell and the network connectivity that accounts for the experimental distribution of common groups of spikelets. (A) Schematics of the modeled network where the recorded pairs of neurons (black and red circles) are connected to four common neurons (purple) and to 12 and 15 additional neurons (cyan); 34 other neurons that are connected to either the cyan or the purple neurons are also shown (gray). (B) the four common groups of spikelets recorded in the black and red cells in A. (C) Plot of the predicted number of connections per cell, estimated from the common groups of spikelets, against the real number of connections per cell. The line marks the diagonal, the + sign marks the mean and the pink circles represent the two cells in A. (D-F) the expected distribution of the common groups in a model where the probability of connection is distance- dependent. (D) Schematic illustration of a distance dependent connectivity. The connection probability is color coded. (E) The probability of connection in the model (gray bars) and in the experiments (blue line) as a function of the inter-somatic distance. The blue curve represents a Gaussian fit to the data. (F) Distribution of the common

groups in the model (gray bars) and experiments (green line) for cells of up to 40 um apart. (G-I) Same as D-F for two networks that are organized in clusters of neurons with a high probability of connection within a cluster (continuous line in inset; matching color-code as the bars in H and I) and a low probability between clusters (dashed lines in inset) in both networks. Each cluster consisted of about 40 neurons.

Discussion

In this study, we measured subthreshold unitary activity from neurons of the inferior olive in slice preparation. The implementation of a variety of experimental approaches linked with computational simulation led to several important conclusions regarding the organization of the network of electrically coupled neurons in the inferior olive nucleus. We showed that there are two populations of non-synaptic unitary events that differ in their waveform and amplitude. The spikelets represent the occurrence of action potentials in a coupled neuron, and the IREs are likely to represent intrinsic regenerative responses at remote locations. It should be noted that in the scientific literature the word 'spikelets' refers to all non-synaptic subthreshold unitary events and thus creates a certain lack of consistency regarding their origin (see Introduction). The uniqueness of our experimental system lies in its ability to differentiate between two types of non-synaptic unitary events and thus to characterize them. We then used the spikelets recorded simultaneously from two neurons to gain insights into the size and organization of the electrically coupled network within the IO nucleus. Analysis of the experimental results showed that each olivary neuron is connected to ~ 20 other neurons and theoretical considerations indicate that the nucleus is organized into clusters of neurons, where the probability of connection within a cluster is higher than the probability of connection between clusters.

The Internally Regenerative Events

These fast subthreshold responses are a mystery. At first glance, they appeared to be a representation of an action potential in a coupled cell, and the difference from spikelets could be accounted for satisfactorily by direct versus indirect coupling where the coupling is mediated through an intermediate neuron. The simulations showed that this can explain the different waveforms as well as the amplitude of the two types of responses (see Supplemental information, Figure S3). However, out of over 45 paired recordings we **never** encountered a pair where an action potential in one neuron elicited an IRE in the coupled neuron. Furthermore, an IRE in one neuron never coincided with a spikelet in the other neuron. Moreover, whereas the probability of spikelets was independent of the membrane voltage, the IRE showed an increased probability at depolarization (Figure 3). Finally, IREs were recorded from the olivary neuron in CX 36 knockout mice (De Zeeuw *et al.*, 2003)(see Supplemental information, Figure S1). Thus, we concluded that the large unitary events represent localized regenerative responses at remote cellular locations.

The locations and mechanism of generation of the IREs are not completely resolved. A localized regenerative response requires a localized concentration of voltage-dependent channels that can support the generation of a local action potential. We investigated three possible locations: 'hotspots' along the dendritic tree, spike generation at different Nodes of Ranvier along the axon, and spike generation at spines located along the axon initial segment. All three possibilities can support the occurrence of unitary events of different amplitudes and almost identical waveforms and can account for the voltage dependency of the waveform. However, the locations of the

461 dendritic hot spots, which can support similar waveform with different amplitudes, are restricted
462 to rather small dendritic segments distributed on different dendritic branches without any
463 common structural features. Thus, it is difficult to envisage a sophisticated mechanism that
464 determines the location of the voltage-dependent ionic channels within a rather large dendritic
465 tree that enables the generation of action potentials **solely** at the designated locations. Finally, a
466 full action potential at the dendritic tree should be able to propagate through the gap-junctions
467 to the post junctional neurons and thus should be revealed during paired recordings.
468 The Nodes of Ranvier, on the other hand, are well-organized sites where the locations of the
469 voltage-dependent ionic channels are restricted to small patches organized along the axon at
470 similar intervals (Murtie, Macklin and Corfas, 2007). This type of organization is well suited to
471 generate, at somatic level, a set of subthreshold events organized in well-defined groups of
472 different amplitudes. The almost identical waveform of such events reflects the very low
473 capacitance of the axon (due to the myelin sheet), which prevents waveform changes. However,
474 to account for the failure of axonal propagation, one has to assume that action potentials can be
475 generated down the axon away from the cell body (Pinault, 1995; Sasaki, 2013). Moreover, the
476 fact that the axon, or more likely the axon initial segment, is usually regarded as the site with the
477 lowest threshold (Palmer and Stuart, 2006), cannot be readily applied in our case, since
478 simultaneous failure at multiple nodes are needed to generate different amplitudes.
479 Finally, we were able to simulate the experimental observation assuming that the source of the
480 IREs are the spines that emerge from the axon initial segment. If these spines can support action
481 potentials, as suggested in other systems (Segev and Rall, 1998; Araya *et al.*, 2007; Bywalez *et al.*,
482 2015), it should appear at the somatic level as an IRE. In our model, the different amplitudes

mostly reflect the neck length. In fact, the detailed ultrastructural study by De Zeeuw and colleagues (De Zeeuw *et al.*, 1990) indicated that up to 8 spines emerge from the axon initial segment of some olive neurons. Furthermore, these spines are innervated by chemical synapses, where the specific activation of individual spines are bound to occur. Thus, it is more likely that the source of the IREs are these axonal spines.

Spines emerging from an axon is not a common feature of central neurons. As we demonstrated, IREs are strong enough to activate the neurons (Figure 4) and thus generate a unique situation where the activation of the neuron is independent of the background synaptic activity that takes place in the soma and the dendritic tree. It is tempting to speculate that this arrangement ensures activation of the neurons in a state of "emergencies". Thus, when the system is in need of a fast response, it activates these inputs that bypass the ongoing activity, thus insuring an immediate response.

The electrically coupled network in the ***olivary nucleus***

Spikelets and subthreshold oscillations: The formation of electrically coupled network within the olivary nucleus is well-established. Here we suggested that this network, operating as a synchronous rhythmic device, is capable of generating precise temporal patterns (Jacobson, Rokni and Yarom, 2008). Both synchronicity and rhythmicity are generated by the delicate interplay between electrical coupling and ionic conductances. Thus, a single cell by itself cannot oscillate, whereas in a network formation the neurons generate subthreshold oscillations (Manor *et al.*, 1997; Loewenstein, Yarom and Sompolinsky, 2001; Chorev, Yarom and Lampl, 2007). In this work, we studied the relationship between spikelets and subthreshold oscillatory activity and found that in oscillating cells the occurrence of spikelets coincided with the depolarizing phase

505 of the oscillation whereas in non-oscillating cells they seemed to be randomly distributed (Figure
506 2). This result strongly supports our previous hypothesis that the occurrence of subthreshold
507 oscillations is a network phenomenon. Therefore, when the recording cell is oscillating, the entire
508 network is synchronously oscillating, thus generating action potentials at the peak of the
509 oscillation that appear in the recorded cell as spikelets. Theoretically, by calculating the number
510 of spikelets at the peak of the oscillatory activity, one should be able to calculate the number of
511 coupled neurons in the oscillating network. Although tempting, this is practically impossible
512 because spikelets, given their small amplitude and noisy environment, cannot be classified into
513 groups. Therefore, we used the common spikelets to estimate the number of coupled neurons.
514 *Common spikelets:* Recording from two olivary neurons revealed spikelets that occurred
515 simultaneously in both recorded neurons. Given that the average rate of spikelets is 0.56±0.62Hz,
516 the probability that these common spikelets reflect random occurrence is extremely low.
517 Furthermore, the repeated appearance of common spikelets with the same relationships
518 (amplitude ratio and waveforms) further supports the non-random occurrence of these events.
519 Thus, the accurate timing of common spikelets can only be attributed to a common source; i.e.,
520 a single pre-junctional neuron. The number of neurons that were coupled to the two recorded
521 neurons, which varied from 1 to 7, should be correlated with the size of the network; more
522 common spikelets are expected in larger interconnected networks.
523 Our simple method of calculating the size of a coupled network is based on data obtained during
524 simultaneous recordings from two neurons and on the assumption that the neurons display a
525 similar rate of spontaneous spiking activity. Our simulations show that the accuracy of this
526 method is mainly affected by variability in the firing rate (Supplemental information, Figure S2).

To minimize the error in estimating the firing rate of the neurons in the network, we used only the spontaneous rate of the common spikelets, and not the firing rates in the recorded neurons that are affected by the intracellular recordings. Under this assumption, we showed that neurons are connected to 3-40 other neurons. This is in line with other studies reporting 1-38 (Hoge *et al.*, 2011) or 0-33 (Placantonakis *et al.*, 2006) dye coupled neurons. This broad variability can be attributed to the use of an in- vitro system, where differences in the number of cells and the integrity of the circuit are characteristic features. Alternatively, this large variability might reflect an innate feature of the IO nucleus where electrical coupling is under continuous modulation (Lefler, Yarom and Uusisaari, 2014; Mathy, Clark and Häusser, 2014; Turecek *et al.*, 2014).

In addition to calculating the number of connected cells, the distribution of common spikelets enabled us to study the connectivity profile within the nucleus. Our data showed that each two neurons had 1-7 common groups, and a normal distribution with an average of 3-4 groups. However, there was a large number of paired recordings that failed to show common groups. Using a theoretical approach, we demonstrated that this distribution should not be expected if we assume that the probability of connection depends solely on the distance between the neurons. On the other hand, if the nucleus is organized into clusters where the probability of connection within the cluster is higher than between clusters, the observed distribution of common groups can be reproduced. Although the size of the clusters, as well as the probability of connection cannot be defined with the current data, this constitutes the first physiological study that supports the assumption of clustered organization of the nucleus deduced mainly from morphological studies.

548 In summary, we presented a comprehensive study that implemented a wide range of research
549 approaches to unravel the functional architecture of the inferior olivary network. We showed
550 that by analyzing spontaneous subthreshold events, new insights into the organization of the
551 network can be gained, thus paving the way for a novel experimental and theoretical approach
552 to the study of electrically-coupled networks.

553

554 ## Acknowledgments

555 This study was supported by the Israel Science Foundation (http://www.isf.org.il/) grant
556 #1496_2016. I.S and O.A were supported by grant agreement no. 604102 'Human Brain Project',
557 a collaborative grant under the Blue Brain Project and a grant from the Gatsby Charitable
558 Foundation. Y.L. was supported by a postdoctoral fellowship from the Edmund and Lily Safra
559 Center for Brain Sciences (ELSC).

560

561 ## Author contributions

562 These authors contributed equally: Y. Lefler and O. Amsalem
563 Experimental work and data analysis were conducted by Y.L, and computational work and data
564 analysis by O.A. All authors interpreted the data and wrote the manuscript.

565

566 ## Declaration of Interests

567 The authors declare no competing interests.

568

Materials and Methods

Animals

All experimental procedures were approved by the Hebrew University's Animal Care and Use Committee. Brain stem slices were prepared from the following strains of mice: C57BL/6, B6.Cg-Tg (Thy1-COP4/EYFP)(Jackson Laboratory) and Gad2-tm2(cre)Zjh/J (Jackson Laboratory).

Slice preparation

Mice were anesthetized with an intraperitoneal injection of Pentobarbital (60mg/Kg), and 300 µm coronal brainstem slices containing the inferior olive were dissected using a Campden 700smz slicer (Campden Instruments), in 35˚c physiological solution containing 126 mM NaCl, 3 mM KCl, 1.3mM $MgSO_4$, 1.2mM KH_2PO_4, 26mM $NaHCO_3$, 10mM glucose, and 2.4mM $CaCl_2$, gassed with 95% O_2 and 5% CO_2. Slices were left in physiological solution at 35˚c for 0.5 - 8 hours until transferred to the recording chamber.

Electrophysiological recordings and ChR stimulation

The recording chamber was perfused with 95% O_2 and 5% CO_2 physiological solution at 24˚c–28˚c. Slices were visualized using a 40X water-immersion objective in an Olympus BX61WIF microscope equipped with infrared differential interference contrast (DIC). In order to record from intact olivary networks, recordings were targeted to the deepest neurons possible in the slice. Whole-cell recordings were performed using 6-9 MΩ glass pipettes with intracellular solution containing 4mM NaCl, 10^{-3}mM $CaCl_2$, 140mM K-gluconate, 10^{-2} mM EGTA, 4 mM Mg-ATP, and 10 mM HEPES (pH 7.2). Signals were acquired at 10-20KHz using a Multiclamp 700B (Molecular Devices) and LabView-based custom-made acquisition software (National

590 Instruments and ZerLabs). For the ChR experiments, a custom -made digital mirror light
591 stimulator with a LED light source (460 nm; Prizmatics) was used to activate the ChR at defined
592 locations on the slice. In some experiments either TEA (10 mM), CNQX (10-40 µM), DNQX (20-40
593 µM) and/or AP-5 (40-100 µM) were added to the recording solution or QX-314 (2-10 mM) was
594 added to the pipette intracellular solution.

595 **Reconstructing neurons**

596 In a few experiments (using C57BL/6 mice), Neurobiotin (0.5%; Vector Laboratories) was added
597 to the pipette solution to label the recorded neurons. Slices were then fixed in 4%
598 paraformaldehyde overnight, washed in PBS and stained with 1 µg/ml Streptavidin AlexaFluor
599 488 (Life Technologies).

600 **Data analysis and Statistics**

601 Analysis was performed using MATLAB (R2014b and R2016a, MathWorks) for the experimental
602 data and Python 2.7 for the simulation data. The 71 neurons that were selected for detailed
603 analysis had a frequency of subthreshold events exceeding 0.02 Hz. The events were divided into
604 two different groups according to their amplitude and rise time. The event rise time was
605 calculated as 10%–90% of the amplitude. The IRE groups were clustered using the K-means
606 clustering method. The coupling coefficient (CC, Figure 2) was calculated as the ratio between
607 the change in the steady-state voltage of the post-junctional cell and that of the pre-junctional
608 cell in response to 250 ms current injection in the pre-junctional cell. The spike coupling
609 coefficient was measured as the amplitude of the post-junctional spikelet divided by the
610 amplitude of the pre-junctional action potential. A Pearson correlation was used to calculate the
611 p-value of the linear regression in Figure 2C. The Inter-spikelet-interval (ISLI) in oscillating

612 neurons (Figure 2G) was only calculated in neurons that had more than 150 spikelets during the
613 session. The ISLI histogram was computed using 4 ms time bins, and the autocorrelation in
614 oscillating neurons was calculated using a lag of 1 ms.
615 The effect of the DC current injection in (Figure 3 C-H) was measured in 16 neurons for different
616 values of current injection. For each neuron, the average value for each current injection was
617 calculated (gray dots in Figure 3C-H) and fitted with a linear line (dashed gray lines). To calculate
618 the average slope (black lines), we averaged the gray dots for each current injection (black dots)
619 and fitted them with a linear line. Error bars represent STD. A one-sample t-test was used to
620 compare the distribution of the slopes of the linear fits of each cell (dashed gray lines) to a
621 distribution with a mean equal to zero. A paired t-test was used to test for differences in the
622 effect on spikelets and IREs. The frequency values for spikelets and IREs (Figure 3G-H) were
623 normalized for each cell to the highest value. The normalized IREs frequency (Figure 3H) was
624 calculated from both IREs and the action potentials that were evoked from IREs.
625 To define spikes that were evoked from IREs (Figure 4A-C), we examined the phase plot of all
626 spikes in each cell and manually searched for a clear gap between the curves around the
627 threshold for spike initiation. To isolate the ChR-evoked subthreshold events (Figure 4E), synaptic
628 responses that did not evoke IREs or spikes were averaged and subtracted from individual
629 responses with IREs.

630 Common spikelets (Figure 7) were defined as spikelets that were detected in a paired recording
631 in both cells simultaneously. Groups of common spikelets were clustered using k-means analysis
632 on the peak voltage, followed by manual curation in which we verified that all common spikelets
633 in a group had a similar shape. To estimate the number of connections per cell, the total number

of spikelets ($T_{spikelets}$) was multiplied by the number of groups (N_{groups}) and divided by the number of common spikelets ($C_{spikelets}$):

$$\text{Estimated connections per cell} = \frac{T_{spikelets} * N_{groups}}{C_{spikelets}}$$

If the two recorded cells were coupled (i.e., a spike in one cell gave rise to a spikelet in the other cell), +1 was added to the estimation of connections for these two cells.

Neuron models

Using the Neurolucida software (MBF Bioscience), three olivary neurons were reconstructed from fluorescence image stacks acquired using a Leica TCS SP5 confocal microscope (Leica Microsystems). To compensate for tissue shrinkage, the z-axis of the reconstruction was multiplied by a factor of 3. A compartmental model was generated from the morphological reconstruction using NEURON (Carnevale and Hines, 2006). The axial resistance (R_a) was set to 100 Ωcm, the specific membrane capacitance (C_m) to 1 μF/cm^2 and the specific membrane resistivity (R_m) for the three reconstructed cells were 4300, 4500, 3800 Ωcm^2 respectively. These values were chosen to yield an input resistance (R_{in}) that was within the experimental range (115±43 MΩ).

Axon model

The model was based on a previous axonal model (Chen *et al.*, 2002) (ModelDB, accession number 3793) with some modification. The model had the following compartments: soma, five cylindrical dendrites, an axon hillock (AH), an axon initial segment (AIS), ten myelinated segments and ten Nodes of Ranvier (Node). The dimensions and density of the channel conductances for these compartments are summarized in Table 1 and are partly based on previous EM studies (De

Zeeuw *et al.*, 1990). Blocking of the different nodes was implemented by removing all active conductances at that node (Figure 5). The axial resistance was 150 Ωcm; the specific membrane capacitance (C_m) was 1 µF/cm^2 in all compartments except for the myelinated segments, where the C_m was 0.01 µF/cm^2. The specific membrane resistivity (R_m) was 12,000 Ωcm^2 in all compartments except for the myelinated segments, where R_m was 1,200,000 Ωcm^2 so that the myelin membrane time constant was 12 ms. When the myelin C_m was modified, R_m was set to a value that kept the membrane time constant at 12 ms.

Table 1

	Soma	Dendrites	Axon Hillock (AH)	Axon Initial segment (AIS)	Myelin	Node of Ranvier
Diameter (µm)	20	1.5	2.7 - 1.3	1.3	1.3	1.3
Length (µm)	20	200	18	30	40	2
g_{Na} pS/µm^2	175	0	175	5000	0	5000
g_K pS/µm^2	50.638	0	50.638	300	0	300

Model of axon with spines

Four spines were added to the axon model in the AH, 11.7, 15.3, 4.5 and 8.1 µm from the soma. Each spine had a neck length of 8.5, 4.5, 7, 3.5 µm, respectively, and a diameter of 0.2 µm. The spine head diameter and length were 2 µm each. The sodium and potassium conductances (gNa

and gK, respectively) in the AH and in the spine heads were set as in the AIS (Table 1). For these simulations, the active conductances were removed from the Nodes of Ranvier.

Building the IO network connectivity matrices

We constructed a network of IO composed of 1134 neurons randomly distributed within a volume of 250x500x200 µm, which resulted in 0.045 neurons per 10 μm^3. We then clustered the neurons by their location using k-means clustering, and varied the number of neurons in a cluster by choosing k to be 1134 divided by the number of neurons in a cluster. The probability of a connection between two neurons decays with distance according to a Gaussian profile:

$$\frac{\Sigma * e^{-\frac{x^2}{2*\sigma^2}}}{100}$$

where Σ is the maximal probability for connection (when the distance between the neurons is 0, x is the distance between neurons and σ sets the decay of connection probability with distance (see Figure 8H inset for examples). Note that the shape profile of neuron connectivity within a cluster could have a different Σ and σ than the connectivity profile of neurons belonging to different clusters. The common neighbor distribution (Figure 8F, I) was calculated on randomly selected pairs of neurons within a distance of 40 µm.

Constructing the IO network model

To simulate a realistic network of IO neurons, we followed the steps described above but with a few modifications. The network volume was 125x250x100 µm, and populated with 180 neurons (0.057 neurons for 10 μm^3). These neurons were cloned from the three 3D-reconstructed olivary neurons, one of which is shown in Figure 5. We set the cluster size, k, to 40. Σ and σ were 77 and

688 15 within a cluster and 45 and 20 between clusters, respectively (Figure 8H, inset, gray). The
689 electrical connection between two neurons was mediated by 2 gap junctions (GJs). AGJ
690 conductance (GJc) of 0.3 nS resulted in a coupling coefficient of 0.03±0.019 as in the experimental
691 range (0.039±0.029). After adding GJc to the modeled cell, R_m was modified to maintain the
692 experimental value of R_{in} (See details in (Amsalem *et al.*, 2016)). The spikes in the networks were
693 created by current injection to the soma (simulated spikes) following a Poisson process.

694

695 **References**

696 Amsalem, Oren, Werner Van Geit, Eilif Muller, Henry Markram, and Idan Segev. "From Neuron
697 Biophysics to Orientation Selectivity in Electrically Coupled Networks of Neocortical L2/3
698 Large Basket Cells." Cerebral Cortex 26, no. 8 (2016): 3655–68.
699 https://doi.org/10.1093/cercor/bhw166.

700 Araya, R., V. Nikolenko, K. B. Eisenthal, and R. Yuste. "Sodium Channels Amplify Spine
701 Potentials." Proceedings of the National Academy of Sciences 104, no. 30 (2007): 12347–
702 52. https://doi.org/10.1073/pnas.0705282104.

703 Avoli, Massimo, Mario Methot, and Hiroto Kawasaki. "GABA-Dependent Generation of Ectopic
704 Action Potentials in the Rat Hippocampus [In Process Citation]." European Journal of
705 Neuroscience 10, no. 8 (1998): 2714–22.

706 Bennett, Michael V.L., and R Suzanne Zukin. "Electrical Coupling and Neuronal Synchronization
707 in the Mammalian Brain." Neuron 41, no. 4 (2004): 495–511.
708 https://doi.org/10.1016/S0896-6273(04)00043-1.

Bennett, Michael V.L, and R. Suzanne Zukin. “Electrical Coupling and Neuronal Synchronization in the Mammalian Brain.” Neuron. Cell Press, February 19, 2004. https://doi.org/10.1016/S0896-6273(04)00043-1.

Bloedel, J R, and Timothy J Ebner. “Rhythmic Discharge of Climbing Fiber Afferents in Response to Natural Peripheral Stimuli in the Cat.” The Journal of Physiology 352 (July 1984): 129–46. https://doi.org/10.1017/S0009838810000340.

Buzsáki, György. “Theta Rhythm of Navigation: Link between Path Integration and Landmark Navigation, Episodic and Semantic Memory.” Hippocampus 15, no. 7 (2005): 827–40. https://doi.org/10.1002/hipo.20113.

Bywalez, Wolfgang G., Dinu Patirniche, Vanessa Rupprecht, Martin Stemmler, Andreas V M Herz, Dénes Pálfi, Balázs Rózsa, and Veronica Egger. “Local Postsynaptic Voltage-Gated Sodium Channel Activation in Dendritic Spines of Olfactory Bulb Granule Cells.” Neuron 85, no. 3 (2015): 590–601. https://doi.org/10.1016/j.neuron.2014.12.051.

Carnevale, Nicholas Ted, and Michael L. Hines. The NEURON Book. Cambridge University Press, 2006. https://doi.org/10.1017/CBO9780511541612.

Chen, Wei R., Gongyu Y. Shen, Gordon M. Shepherd, Michael L. Hines, and Jens Midtgaard. “Multiple Modes of Action Potential Initiation and Propagation in Mitral Cell Primary Dendrite.” Journal of Neurophysiology 88, no. 5 (2002): 2755–64. https://doi.org/10.1152/jn.00057.2002.

Chorev, E., Y. Yarom, and I. Lampl. “Rhythmic Episodes of Subthreshold Membrane Potential Oscillations in the Rat Inferior Olive Nuclei in Vivo.” Journal of Neuroscience 27, no. 19

(2007): 5043–52. https://doi.org/10.1523/JNEUROSCI.5187-06.2007.

Chorev, Edith, and Michael Brecht. "In Vivo Dual Intra- and Extracellular Recordings Suggest Bidirectional Coupling between CA1 Pyramidal Neurons." Journal of Neurophysiology 108, no. 6 (2012): 1584–93. https://doi.org/10.1152/jn.01115.2011.

Condorelli, Daniele F., Natale Belluardo, Angela Trovato-Salinaro, and Giuseppa Mudò. "Expression of Cx36 in Mammalian Neurons." Brain Research Reviews 32, no. 1 (2000): 72–85. https://doi.org/10.1016/S0165-0173(99)00068-5.

Connors, Barry W., and Michael A. Long. "Electrical Synapses in the Mammalian Brain." Annual Review of Neuroscience 27, no. 1 (2004): 393–418. https://doi.org/10.1146/annurev.neuro.26.041002.131128.

Connors, Barry W. "Synchrony and so Much More: Diverse Roles for Electrical Synapses in Neural Circuits." Developmental Neurobiology 77, no. 5 (2017): 610–24. https://doi.org/10.1002/dneu.22493.

Coulon, Philippe, and Carole E. Landisman. "The Potential Role of Gap Junctional Plasticity in the Regulation of State." Neuron 93, no. 6 (2017): 1275–95. https://doi.org/10.1016/j.neuron.2017.02.041.

Devor, Anna, and Yosef Yarom. "Electrotonic Coupling in the Inferior Olivary Nucleus Revealed by Simultaneous Double Patch Recordings." Journal of Neurophysiology 87, no. 6 (2002a): 3048–58. https://doi.org/10.1152/jn.00399.2001.

Devor, Anna, and Yosef Yarom. "Generation and Propagation of Subthreshold Waves in a Network of Inferior Olivary Neurons." Journal of Neurophysiology 87, no. 6 (2002b): 3059–

69.

Dugladze, Tamar, Dietmar Schmitz, Miles A Whittington, Imre Vida, and Tengis Gloveli. "Segregation of Axonal and Somatic Activity during Fast Network Oscillations." Science 336, no. June (2012): 1458–61.

Eccles, J. C., R. Llinás, and K. Sasaki. "The Excitatory Synaptic Action of Climbing Fibres on the Purkinje Cells of the Cerebellum." The Journal of Physiology 182, no. 2 (1966): 268–96. https://doi.org/10.1113/jphysiol.1966.sp007824.

Engel, Andreas K., Pascal Fries, and Wolf Singer. "Dynamic Predictions: Oscillations and Synchrony in Top–down Processing." Nature Reviews Neuroscience 2, no. 10 (2001): 704–16. https://doi.org/10.1038/35094565.

Galarreta, Mario, and Shaul Hestrin. "A Network of Fast-Spiking Cells in the Neocortex Connected by Electrical Synapses." Nature 402, no. 6757 (1999): 72–75. https://doi.org/10.1038/47029.

Gibson, Jay R, Michael Belerlein, and Barry W Connors. "Two Networks of Electrically Coupled Inhibitory Neurons in Neocortex." Nature 402, no. 6757 (1999): 75–79. https://doi.org/10.1038/47035.

Giessen, Ruben S. Van Der, Sebastiaan K. Koekkoek, Stijn van Dorp, Jornt R. De Gruijl, Alexander Cupido, Sara Khosrovani, Bjorn Dortland, et al. "Role of Olivary Electrical Coupling in Cerebellar Motor Learning." Neuron 58, no. 4 (2008): 599–612. https://doi.org/10.1016/j.neuron.2008.03.016.

Golding, Nace L, and Nelson Spruston. "Dendritic Sodium Spikes Are Variable Triggers of Axonal

772 Action Potentials in Hippocampal CA1 Pyramidal Neurons." Neuron 21, no. 5 (1998): 1189–
773 1200. https://doi.org/10.1016/S0896-6273(00)80635-2.

774 Hoge, Gregory J, Kimberly G V Davidson, Thomas Yasumura, Pablo E Castillo, John E Rash, and
775 Alberto E Pereda. "The Extent and Strength of Electrical Coupling between Inferior Olivary
776 Neurons Is Heterogeneous." Journal of Neurophysiology 105, no. 3 (2011): 1089–1101.
777 https://doi.org/10.1152/jn.00789.2010.

778 Hormuzdi, Sheriar G, Mikhail A Filippov, Georgia Mitropoulou, Hannah Monyer, and Roberto
779 Bruzzone. "Electrical Synapses: A Dynamic Signaling System That Shapes the Activity of
780 Neuronal Networks." Biochimica et Biophysica Acta - Biomembranes, 2004.
781 https://doi.org/10.1016/j.bbamem.2003.10.023.

782 Hughes, S. W., K. L. Blethyn, D. W. Cope, and V. Crunelli. "Properties and Origin of Spikelets in
783 Thalamocortical Neurones in Vitro." Neuroscience 110, no. 3 (2002): 395–401.
784 https://doi.org/10.1016/S0306-4522(01)00577-2.

785 Jacobson, Gilad A., Dan Rokni, and Yosef Yarom. "A Model of the Olivo-Cerebellar System as a
786 Temporal Pattern Generator." Trends in Neurosciences 31, no. 12 (2008): 617–25.
787 https://doi.org/10.1016/j.tins.2008.09.005.

788 Juszczak, Grzegorz R., and Artur H. Swiergiel. "Properties of Gap Junction Blockers and Their
789 Behavioural, Cognitive and Electrophysiological Effects: Animal and Human Studies."
790 Progress in Neuro-Psychopharmacology and Biological Psychiatry 33, no. 2 (2009): 181–98.
791 https://doi.org/10.1016/j.pnpbp.2008.12.014.

792 Lampl, I, and Y Yarom. "Subthreshold Oscillations and Resonant Behavior: Two Manifestations

of the Same Mechanism." Neuroscience 78, no. 2 (1997): 325–41. https://doi.org/10.1016/S0306-4522(96)00588-X.

Lefler, Yaara, Benjamin Torben-Nielsen, and Yosef Yarom. "Oscillatory Activity, Phase Differences, and Phase Resetting in the Inferior Olivary Nucleus." Frontiers in Systems Neuroscience 7 (2013). https://doi.org/10.3389/fnsys.2013.00022.

Lefler, Yaara, Yosef Yarom, and Marylka Yoe Uusisaari. "Cerebellar Inhibitory Input to the Inferior Olive Decreases Electrical Coupling and Blocks Subthreshold Oscillations." Neuron 81, no. 6 (2014): 1389–1400. https://doi.org/10.1016/j.neuron.2014.02.032.

Leznik, Elena, and Rodolfo Llinas. "Role of Gap Junctions in Synchronized Neuronal Oscillations in the Inferior Olive." Journal of Neurophysiology 94 (2005): 2447–56. https://doi.org/10.1152/jn.00353.2005.

Leznik, Elena, Vladimir Makarenko, and Rodolfo Llinas. "Electrotonically Mediated Oscillatory Patterns in Neuronal Ensembles : An in Vitro Voltage-Dependent Dye-Imaging Study in the Inferior Olive." Journal of Neuroscience 22, no. 7 (2002): 2804–15.

Llinas, R, R Baker, and C Sotelo. "Electrotonic Coupling between Neurons in Cat Inferior Olive." Journal of Neurophysiology 37, no. 3 (1974): 560–71. https://doi.org/10.1152/jn.1974.37.3.560.

Llinás, R R. "Inferior Olive Oscillation as the Temporal Basis for Motricity and Oscillatory Reset as the Basis for Motor Error Correction." Neuroscience 162, no. 3 (2009): 797–804. https://doi.org/10.1016/j.neuroscience.2009.04.045.

Llinas, R, and K Sasaki. "The Functional Organization of the Olivo-Cerebellar System as

814 Examnied by Multiple Purkinje Cell Recordings." European Journal of Neuroscience 1, no.
815 May (1989): 587–602.

816 Llinas, R, and Y Yarom. "Oscillatory Properties of Guinea-Pig Inferior Olivary Neurons and Their
817 Pharmacological Modulation - an in Vitro Study." Journal of Physiology 376 (1986): 163–
818 82.
819 http://links.isiglobalnet2.com/gateway/Gateway.cgi?GWVersion=2&SrcAuth=mekentosj&
820 SrcApp=Papers&DestLinkType=FullRecord&DestApp=WOS&KeyUT=A1986D283500010%5
821 Cnpapers3://publication/uuid/38D999FC-31EF-4056-A40A-E84265A428D3.

822 Loewenstein, Y., Y. Yarom, and H. Sompolinsky. "The Generation of Oscillations in Networks of
823 Electrically Coupled Cells." Proceedings of the National Academy of Sciences 98, no. 14
824 (2001): 8095–8100. https://doi.org/10.1073/pnas.131116898.

825 Lou, J S, and James R Bloedel. "Responses of Sagittally Aligned Purkinje Cells during Perturbed
826 Locomotion: Synchronous Activation of Climbing Fiber Inputs." Journal of Neurophysiology
827 68, no. 2 (1992): 570–80. https://doi.org/10.1152/jn.1992.68.2.570.

828 MacVicar, B., and F. Dudek. "Electrotonic Coupling between Pyramidal Cells: A Direct
829 Demonstration in Rat Hippocampal Slices." Science 213, no. 4509 (1981): 782–85.
830 https://doi.org/10.1126/science.6266013.

831 Mann-Metzer, P, and Yosef Yarom. "Electrotonic Coupling Interacts with Intrinsic Properties to
832 Generate Synchronized Activity in Cerebellar Networks of Inhibitory Interneurons." The
833 Journal of Neuroscience 19, no. 9 (1999): 3298–3306.
834 https://doi.org/10.1523/JNEUROSCI.19-09-03298.1999.

835 Manor, Y, J Rinzel, I Segev, Y Yarom, L. S. Benardo, R. E. Foster, J.-P. Benitah, et al. “Low-
836 Amplitude Oscillations in the Inferior Olive: A Model Based on Electrical Coupling of
837 Neurons with Heterogeneous Channel Densities.” Journal of Neurophysiology 77, no. 5
838 (1997): 2736–52. https://doi.org/10.1016/0361-9230(86)90089-4.

839 Marder, Eve, Gabrielle J Gutierrez, and Michael P Nusbaum. “Complicating Connectomes :
840 Electrical Coupling Creates Parallel Pathways and Degenerate Circuit Mechanisms,” 2016.
841 https://doi.org/10.1002/dneu.22410.

842 Mathy, Alexandre, Beverley A. Clark, and Michael Häusser. “Synaptically Induced Long-Term
843 Modulation of Electrical Coupling in the Inferior Olive.” Neuron 81, no. 6 (2014): 1290–96.
844 https://doi.org/10.1016/j.neuron.2014.01.005.

845 Michalikova, Martina, Michiel W.H. Remme, and Richard Kempter. “Spikelets in Pyramidal
846 Neurons: Action Potentials Initiated in the Axon Initial Segment That Do Not Activate the
847 Soma.” PLoS Computational Biology 13, no. 1 (2017): 1–25.
848 https://doi.org/10.1371/journal.pcbi.1005237.

849 Mukamel, Eran A, Axel Nimmerjahn, and Mark J Schnitzer. “Automated Analysis of Cellular
850 Signals from Large-Scale Calcium Imaging Data.” Neuron 63, no. 6 (2009): 747–60.
851 https://doi.org/10.1016/j.neuron.2009.08.009.

852 Murtie, Joshua C, Wendy B Macklin, and Gabriel Corfas. “Morphometric Analysis of
853 Oligodendrocytes in the Adult Mouse Frontal Cortex.” Journal of Neuroscience Research
854 85 (2007): 2080–86. https://doi.org/10.1002/jnr.

855 O’brien, John. “The Ever-Changing Electrical Synapse.” Current Opinion in Neurobiology 0

(2014): 64–72. https://doi.org/10.1111/j.1743-6109.2008.01122.x.Endothelial.

Ozden, I., M. R. Sullivan, H. M. Lee, and S. S.-H. Wang. “Reliable Coding Emerges from Coactivation of Climbing Fibers in Microbands of Cerebellar Purkinje Neurons.” Journal of Neuroscience 29, no. 34 (2009): 10463–73. https://doi.org/10.1523/JNEUROSCI.0967-09.2009.

Palmer, Lucy M., and Greg J. Stuart. “Site of Action Potential Initiation in Layer 5 Pyramidal Neurons.” Journal of Neuroscience 26, no. 6 (2006): 1854–63. https://doi.org/10.1523/JNEUROSCI.4812-05.2006.

Pinault, Didier. “Backpropagation of Action Potentials Generated at Ectopic Axonal Loci: Hypothesis That Axon Terminals Integrate Local Environmental Signals.” Brain Research Reviews 21, no. 1 (1995): 42–92. https://doi.org/10.1016/0165-0173(95)00004-M.

Placantonakis, Dimitris G, Anatoly A Bukovsky, Sue A Aicher, Hans-Peter Kiem, and John P Welsh. “Continuous Electrical Oscillations Emerge from a Coupled Network: A Study of the Inferior Olive Using Lentiviral Knockdown of Connexin36.” Journal of Neuroscience 26, no. 19 (2006): 5008–16. https://doi.org/10.1523/JNEUROSCI.0146-06.2006.

Rall, Wilfrid. “Distinguishing Theoretical Synaptic Potentials Computed for Different Soma-Dendritic Distributions of Synaptic Input.” Journal of Neurophysiology, 1967, 1138–68.

Ritz, R, and T J Sejnowski. “Synchronous Oscillatory Activity in Sensory Systems: New Vistas on Mechanisms.” Current Opinion in Neurobiology 7 (1997): 536–46.

Sasaki, Takuya. “The Axon as a Unique Computational Unit in Neurons.” Neuroscience Research 75, no. 2 (2013): 83–88. https://doi.org/10.1016/j.neures.2012.12.004.

877 Schmitz, Dietmar, Sebastian Schuchmann, Andre Fisahn, Andreas Draguhn, Eberhard H Buhl,
878 Elisabeth Petrasch-Parwez, Rolf Dermietzel, Uwe Heinemann, and Roger D Traub. “Axo-
879 Axonal Coupling: A Novel Mechanism for Ultrafast Neuronal Communication.” Neuron 31,
880 no. 5 (2001): 831–40. https://doi.org/10.1016/S0896-6273(01)00410-X.

881 Scholl, Benjamin, Sari Andoni, Nicholas J Priebe, and Nicholas J Priebe. “Functional
882 Characterization of Spikelet Activity in the Primary Visual Cortex.” Journal of Physiology 22
883 (2015): 1–32. https://doi.org/10.1113/JP270876.This.

884 Schultz, S. R., K. Kitamura, A. Post-Uiterweer, J. Krupic, and M. Hausser. “Spatial Pattern Coding
885 of Sensory Information by Climbing Fiber-Evoked Calcium Signals in Networks of
886 Neighboring Cerebellar Purkinje Cells.” Journal of Neuroscience 29, no. 25 (2009): 8005–
887 15. https://doi.org/10.1523/JNEUROSCI.4919-08.2009.

888 Segev, Idan, and Wilfrid Rall. “Excitable Dendrites and Spines: Earlier Theoretical Insights
889 Elucidate Recent Direct Observations.” Trends in Neurosciences 21, no. 11 (1998): 453–60.
890 https://doi.org/10.1016/S0166-2236(98)01327-7.

891 Sheffield, Mark E.J., Tyler K Best, Brett D Mensh, William L Kath, and Nelson Spruston. “Slow
892 Integration Leads to Persistent Action Potential Firing in Distal Axons of Coupled
893 Interneurons.” Nature Neuroscience 14, no. 2 (2011): 200–209.
894 https://doi.org/10.1038/nn.2728.

895 Smith, Spencer L., Ikuko T. Smith, Tiago Branco, and Michael Häusser. “Dendritic Spikes
896 Enhance Stimulus Selectivity in Cortical Neurons in Vivo.” Nature 503, no. 7474 (2013):
897 115–20. https://doi.org/10.1038/nature12600.

898 Sotelo, C, R Llinas, and R Baker. “Structural Study of Inferior Olivary Nucleus of the Cat:
899 Morphological Correlates of Electrotonic Coupling.” Journal of Neurophysiology 37 (1974):
900 541–59. https://doi.org/10.1152/jn.1974.37.3.541.

901 Spencer, W A, and E R Kandel. “Electrophysiology of Hippocampal Neurons: IV. Fast
902 Prepotentials.” Journal of Neurophysiology 24, no. 3 (1961): 272–85.
903 https://doi.org/10.1152/jn.1961.24.3.272.

904 Stasheff, S F, M Hines, and W a Wilson. “Axon Terminal Hyperexcitability Associated with
905 Epileptogenesis in Vitro. I. Origin of Ectopic Spikes.” Journal of Neurophysiology 70, no. 3
906 (1993): 961–75. https://doi.org/10.1152/jn.1993.70.3.976.

907 Steriade, M. “Grouping of Brain Rhythms in Corticothalamic Systems.” Neuroscience 137, no. 4
908 (2006): 1087–1106. https://doi.org/10.1016/j.neuroscience.2005.10.029.

909 Traub, R D, S B Colling, and J G R Jefferys. “Cellular Mechanisms of 4-Aminopyridine-Induced
910 Synchronized after-Discharg Es in the Rat Hippocampal Slice.” J Physiol (Lond) 489, no. 1
911 (1995): 127–40.

912 Traub, Roger D, Andreas Draguhn, Miles A Whittington, Torsten Baldeweg, Andrea Bibbig,
913 Eberhard H. Buhl, and Dietmar Schmitz. “Axonal Gap Junctions between Principal Neurons:
914 A Novel Source of Network Oscillations, and Perhaps Epileptogenesis.” Reviews in the
915 Neurosciences 13, no. 1 (2002): 1–30. https://doi.org/10.1515/REVNEURO.2002.13.1.1.

916 Turecek, Josef, Genevieve S. Yuen, Victor Z. Han, Xiao Hui Zeng, K. Ulrich Bayer, and John P.
917 Welsh. “NMDA Receptor Activation Strengthens Weak Electrical Coupling in Mammalian
918 Brain.” Neuron 81, no. 6 (2014): 1375–88. https://doi.org/10.1016/j.neuron.2014.01.024.

Uhlhaas, Peter J., Gordon Pipa, Bruss Lima, Lucia Melloni, Sergio Neuenschwander, Danko Nikolic, and Wolf Singer. “Neural Synchrony in Cortical Networks: History, Concept and Current Status.” Frontiers in Integrative Neuroscience 3 (2009): 1–19. https://doi.org/10.3389/neuro.07.

Valiante, T A, J L Perez Velazquez, S S Jahromi, and P L Carlen. “Coupling Potentials in CA1 Neurons during Calcium-Free-Induced Field Burst Activity.” The Journal of Neuroscience : The Official Journal of the Society for Neuroscience 15, no. 10 (1995): 6946–56. http://www.ncbi.nlm.nih.gov/pubmed/7472451.

Vigmond, Edward J, J L Perez Velazquez, Taufik A Valiante, Berj L Bardakjian, and Peter L Carlen. “Mechanisms of Electrical Coupling between Pyramidal Cells.” Journal of Neurophysiology 78, no. 6 (1997): 3107–16. https://doi.org/10.1152/jn.1997.78.6.3107.

Wang, X.-J. “Neurophysiological and Computational Principles of Cortical Rhythms in Cognition.” Physiological Reviews 90, no. 3 (2010): 1195–1268. https://doi.org/10.1152/physrev.00035.2008.

Welsh, John P., Eric J. Lang, Izumi Suglhara, and Rodolfo Llinás. “Dynamic Organization of Motor Control within the Olivocerebellar System.” Nature 374, no. 6521 (1995): 450–53. https://doi.org/10.1038/374453a0.

Welsh, John P, and R Llinás. “Some Organizing Principles for the Control of Movement Based on Olivocerebellar Physiology.” Progress in Brain Research 114 (1997): 449–61. https://doi.org/10.1016/S0079-6123(08)63380-4.

Zeeuw, C I De, T J H Ruigrok, J C Holstege, M P A Schalekamp, and J Voogd. “Intracellular

940 Labeling of Neurons in the Medial Accessory Olive of the Cat: III. Ultrastructure of Axon
941 Hillock and Initial Segment and Their GABAergic Innervation." The Journal of Comparative
942 Neurology 300 (1990): 495–510.

943 Zeeuw, Chris I. De, Freek E Hoebeek, Laurens W.J. Bosman, Martijn Schonewille, Laurens
944 Witter, and Sebastiaan K. Koekkoek. "Spatiotemporal Firing Patterns in the Cerebellum."
945 Nature Reviews Neuroscience 12, no. 6 (2011): 327–44. https://doi.org/10.1038/nrn3011.

946 Zeeuw, Chris I De, Edilzh Chorev, Anna Devor, Yait Manor, Ruben S Van Der Giessen, Marcel T
947 De Jeu, Casper C Hoogenraad, et al. "Deformation of Network Connectivity in the Inferior
948 Olive of Connexin 36-Deficient Mice Is Compensated by Morphological and
949 Electrophysiological Changes at the Single Neuron Level." The Journal of Neuroscience 23,
950 no. 11 (2003): 4700–4711. https://doi.org/23/11/4700 [pii].

951

952

953

Supplementary Figures

Figure S1

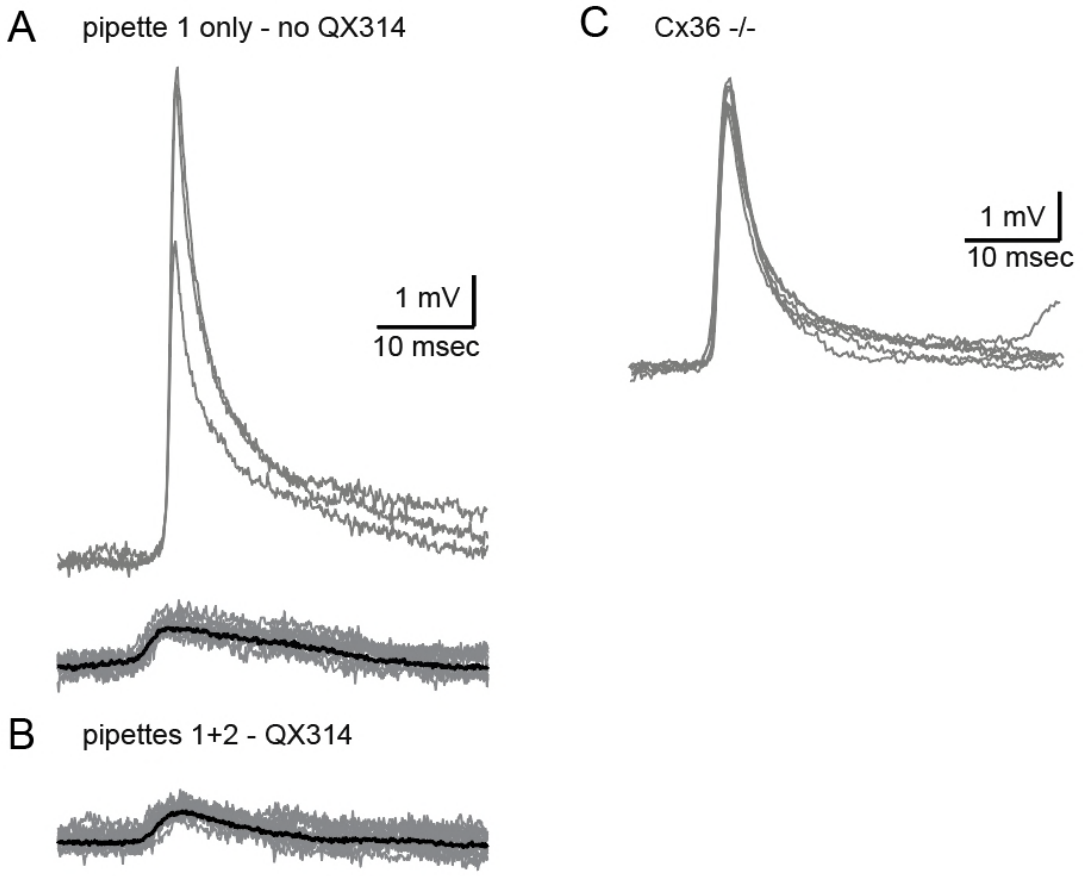

Figure S1. Related to Figure 4. The fast events are Internally Regenerative Events that are independent of gap junctions. (A) IREs (upper traces) and spikelets (lower traces) recorded from an olivary neuron with a regular internal solution. (B) breaking into the cell with another pipette, filled with intracellular solution + 2 mM QX 314, shows that with QX 314, IREs could not be detected while the spikelets' shape and frequency were unaffected. (C) IREs recorded in CX 36 knockout mice showing that IREs can be generated in the absence of gap junctions.

Figure S2

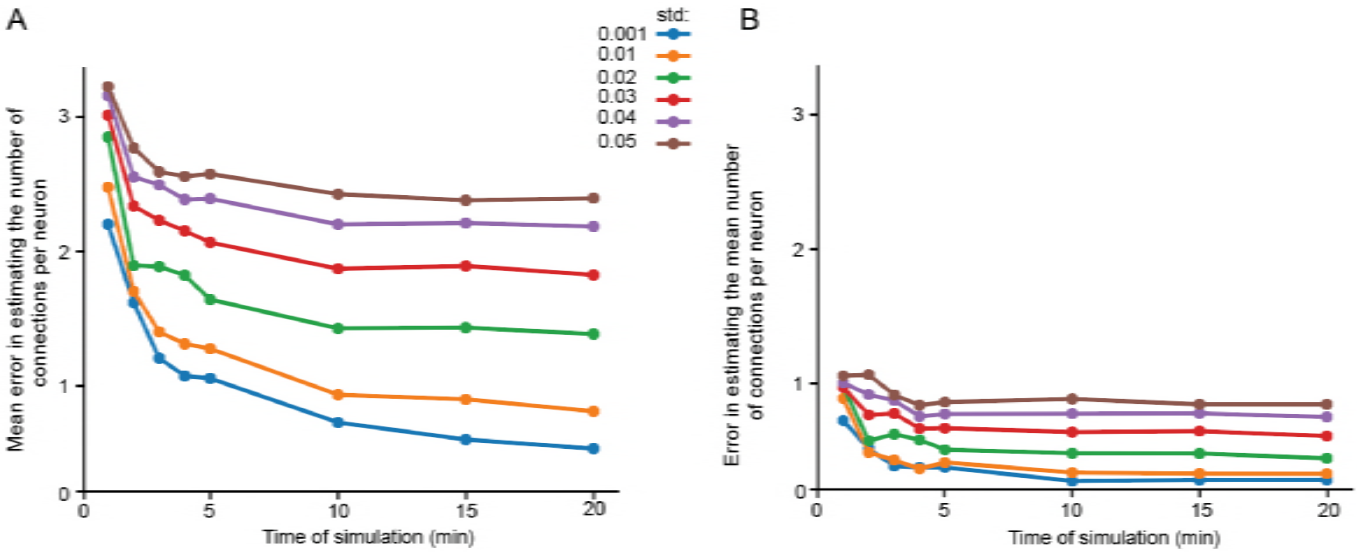

Figure S2. Related to Figure 8. The accuracy in estimating the number of connected neurons is strongly dependent on the variability in firing rate and the simulation duration. (A) difference between the estimated and real number of connections per neurons as a function of simulation duration for 6 different firing rate variabilities (std), color-coded as in the legend. (B) error in estimating the mean number of connections in the network (plus sign in Figure 8C) as a function of simulation duration for 6 different firing rate variabilities (std). The calculation was done only on neurons that had common neighbors (n=278 pairs). Mean firing rate was 0.058 Hz.

Figure S3

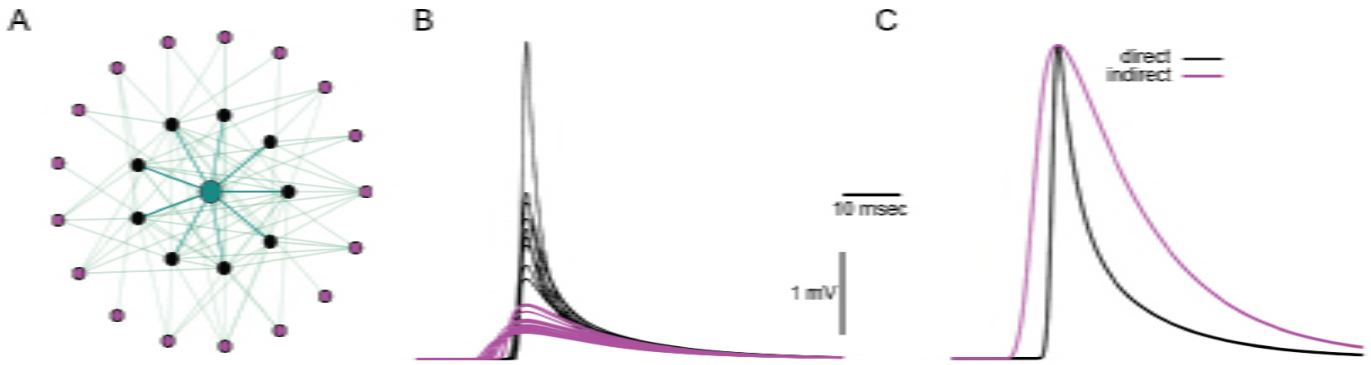

Figure S3. Related to Figure 5 and Figure 6. Difference in events waveform can be attributed to spikes form directly and indirectly connected cells. (A) modelled IO network in which a green cell was connected directly to 9 other cells (black circles), and indirectly to 17 other cells (purple circle). (B) spikelets in this cell due to spikes in directly connected cells (black traces) or indirectly connected cells (purple traces). (C) average normalized spikelets from B. This network is similar to the network in Figure 8A, with two modification - the number of GJs was changed to 6 and the GJc to 0.25 nS.